NASA Contractor Report 3788

Abrasion by Aeolian Particles: Earth and Mars

R. Greeley, S. Williams, B. R. White,
J. Pollack, J. Marshall, and D. Krinsley

GRANTS NSG-2284 and NCC2-60
MARCH 1984

NASA

NASA Contractor Report 3788

Abrasion by Aeolian Particles: Earth and Mars

R. Greeley
Arizona State University
Tempe, Arizona

J. Pollack
NASA Ames Research Center
Moffett Field, California

S. Williams
University of Santa Clara
Santa Clara, California

J. Marshall and D. Krinsley
Arizona State University
Tempe, Arizona

B. R. White
University of California at Davis
Davis, California

Prepared for
NASA Office of Space Science and Applications
under Grants NSG-2284 and NCC2-60

NASA
National Aeronautics
and Space Administration

Scientific and Technical
Information Office

1984

TABLE OF CONTENTS

1. INTRODUCTION

> "Under the stimulus of aridity, wind scour becomes an erosive agent more constant than the rain, more potent than streams, and more persistent than the sea".

So wrote A.K. Lobeck (1939) in his introductory textbook on geomorphology. On Earth, aeolian processes are particularly important in hot and cold deserts, along many coastlines, and in glacial outwash plains. Mars experiences frequent dust storms and lacks the inhibiting effects of liquid water and vegetation. Thus, aeolian processes play an important role in the geological evolution of the surfaces of both Earth and Mars.

The objective of our investigation was to determine rates of wind abrasion for a wide range of conditions on Earth and Mars. The study, however, was restricted to considerations of rock abrasion and does not include deflation or the erosion of landforms.

In order to determine rates of aeolian abrasion, knowledge of three factors is required (Fig. 1): (a) wind characteristics, (b) particle characteristics, and (c) target characteristics. Wind characteristics include wind strengths, durations, and directions. Particle characteristics include particle size, shape, and composition and the velocities and trajectories of windblown grains; the latter two are functions of freestream wind speeds and heights above the ground. Target characteristics include the rock shape and a measure of the resistance of the rock to abrasion, termed the *susceptibility to abrasion*. The rate of abrasion may then be calculated as

$$\text{rate} = (S_a)(q)(f) \qquad (1)$$

where S_a is the susceptibility to abrasion, q is particle flux, and f is wind frequency.

Although many previous studies have addressed wind abrasion, most analyses have lacked various critical elements and are therefore difficult to use in determining rates of wind abrasion. For example, engineering studies of abrasion are generally well documented and quantitative in the approach, but do not involve geological materials such as rocks. On the other hand, studies of wind-abraded rocks – ventifacts – in the natural field environment generally lack sufficient wind frequency data and particle flux information to quantify the results.

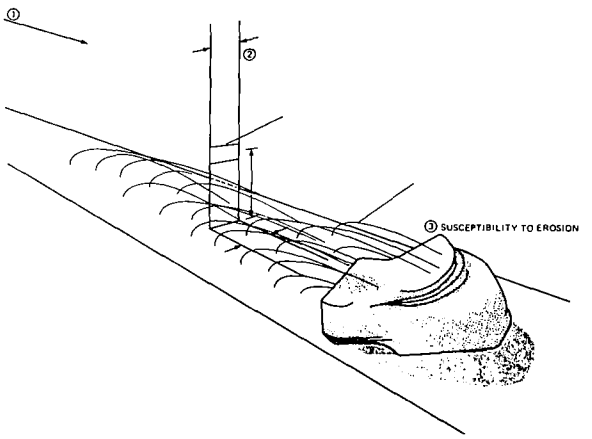

Figure 1. Diagram showing the three principal parameters involved in determining rates of aeolian abrasion: (1) wind factors, including wind velocity, duration and direction; (2) particle characteristics, including sizes, velocities, and fluxes as functions of wind speed and height above the ground, and (3) a measure of the resistance to abrasion of various rocks, termed the susceptibility to abrasion (from Greeley et al., 1982).

TABLE 1. Nomenclature

a_m	maximum impact contact radius	u_f	final particle speed
A	particle cross-sectional area	u_*	wind friction speed
C_D	coefficient of drag	u_{*t}	threshold wind friction speed
C_L	coefficient of lift	u_∞	freestream wind speed
D	drag force	v	wind speed
D_H	mean crack diameter	v_p	particle speed
D_p	particle diameter	v_r	relative speed between particle and wind
E	subscript denoting Earth	w_i	initial particle upward velocity
f	wind frequency	$\bar{w}_i$	average initial particle upward velocity
g	acceleration due to gravity	w_f	final particle downward velocity
G_o	number of saltating grains landing in a unit area per unit time	$\dot{x}$	velocity in x-direction
H	maximum height above surface of saltation trajectory	$\ddot{x}$	acceleration in x-direction
KE	kinetic energy	$\dot{y}$	velocity in y-direction
L	saltation path length	$\ddot{y}$	acceleration in y-direction
L_F	lift force	z	height above surface
m_p	particle mass	z_o	surface roughness
M	subscript denoting Mars	α	angle between saltation trajectory and horizontal surface at impact
Δp	pressure difference	θ	angle subtended by crack 'horns' (Fig. 23)
P_a	atmospheric pressure	λ	average saltation path length
q	saltation area flux gm/cm^2•sec	ρ_a	density of atmosphere
Q	saltation lane flux gm/cm•sec	ρ_p	density of particle
S_a	susceptibility to abrasion	τ_o	total surface shear stress
t	time	τ_s	surface shear due to particle impact
u	wind speed	τ_t	surface wind shear maximum value (at threshold)
u_i	initial particle speed	τ_w	surface wind shear
$C_E, C_M, K_1, K_2, K_3, \xi$			constants

In this study, we have attempted to gain sufficient information on the characteristics of windblown particles, wind frequencies, and material properties appropriate for estimating rates of wind abrasion on Earth and Mars.

1.1 THE MARTIAN DILEMMA

Surface markings have been observed telescopically on Mars for several hundred years. One of the earliest observations that some markings varied seasonally was made in 1884 by the French astronomer E. Trouvelot who attributed the variations to seasonal changes of vegetation (Veverka and Sagan, 1974). Speculations that the markings were related to vegetation, water, or even martian civilizations persisted well into the twentieth century. None of these speculations has been shown to be valid. The first consideration of the markings being related to aeolian processes was apparently made by Dean McLaughlin (1954), who published a series of papers on potential martian wind activity, but it remained for Sagan and Pollack (1969) to first fully propose this idea.

In 1971 the Mariner 9 orbiter and the Soviet spacecraft Mars 2 and 3 arrived at Mars during a major global dust storm and verified the predictions of aeolian activity. In addition to providing information on the dynamics of dust clouds, the Mariner 9 cameras revealed abundant surface features attributed to aeolian processes (McCauley, 1973). Yardangs, dune fields, and various deflation features were identified, along with bright and dark surface patterns that changed their size, shape, and position during the ~11 month mission (Sagan et al., 1972). These patterns (Fig. 2) were correctly interpreted as representing aeolian erosion and deposition. It was concluded from Mariner 9 that the seasonal variations in surface markings were the consequence of major dust storms.

Ultraviolet and infrared spectrometers on board Mariner 9 also provided information on the atmosphere, including chemical composition, temperature, and density. The atmosphere was found to be composed predomi-

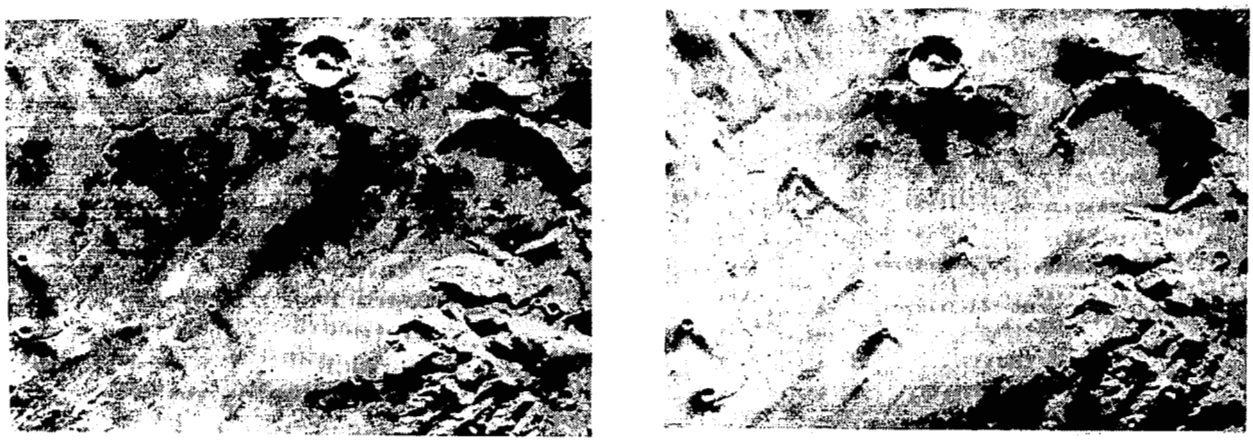

Figure 2. Mars is subject to frequent wind storms which cause changes on the surface, as shown by the variable features *in these Viking orbiter images. Variable features are defined (Sagan et al., 1972) as surface markings that change their size, shape and/or appearance, such as the dark streaks associated with craters visible here in the Daedalia region on Mars (30°S, 118°W). In (a) streaks record winds from the upper left (VO frame 56A41); (b) shows same area for another season in which streaks have two prominent orientations (VO frame 603A08) (from Thomas and Veverka, 1979).*

nantly of carbon dioxide with a density very low compared to Earth. In this low atmospheric density, threshold wind speeds are more than an order of magnitude higher on Mars than on Earth (Fig. 3). Because of these high winds, it was reasoned that windblown particles would also travel much faster on Mars than on Earth and would be very effective agents of abrasion, on a per impact basis. This consideration, coupled with the frequent dust storms, led to predictions of extremely high rates of aeolian erosion (Sagan, 1973; Henry, 1975).

A simple qualitative experiment was run in our wind tunnel (Greeley et al., 1981) to compare wind erosion on Earth and Mars (Fig. 4). In the Earth case, a small front-surface mirror was positioned downwind from a patch of sand. The tunnel wind velocity was increased to achieve particle threshold speed and was maintained until all of the sand was blown away. The experiment was duplicated with a fresh mirror in a simulated martian atmospheric environment of about 7 mb pressure. Again, the wind velocity was just above threshold speed, but because of the low atmospheric density, the threshold speed was

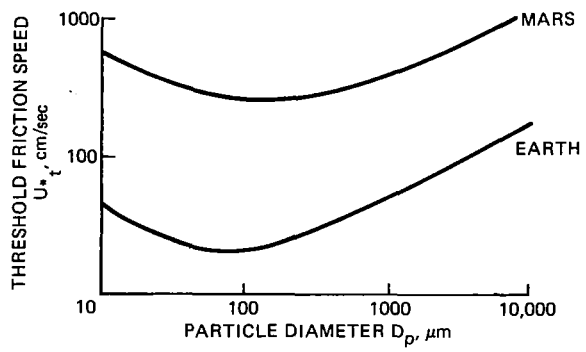

Figure 3. Threshold curves for Earth and Mars showing threshold friction speeds required for particles of different sizes; about a factor of 10 higher speeds are required on Mars than on Earth because of the lower density atmosphere on Mars. The particle size most easily moved (lowest friction speed) is about 80 μm on Earth and about 100 μm on Mars (after Iversen et al., 1976; and Greeley et al., 1980).

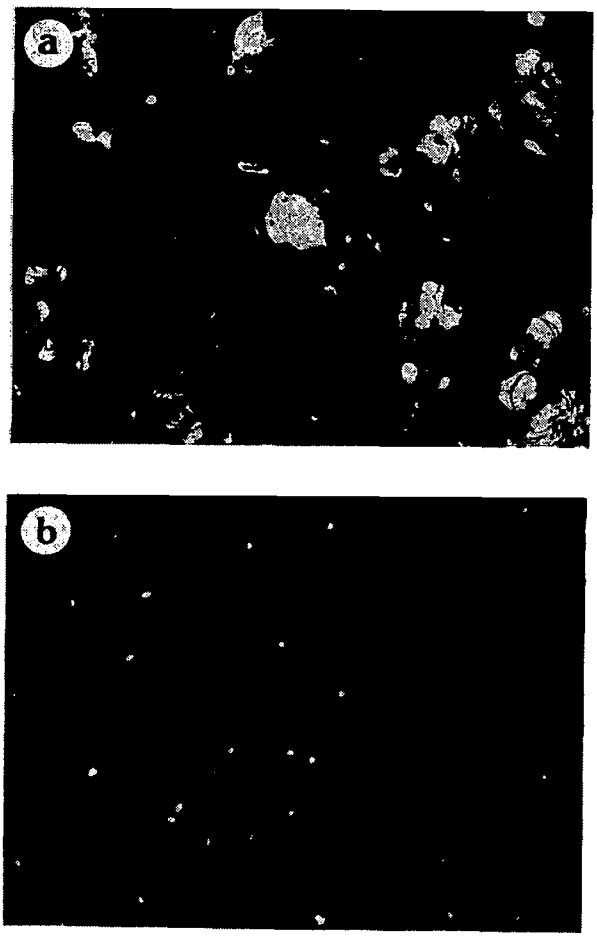

Figure 4. Qualitative comparison of aeolian abrasion on Mars (a) and Earth (b); mirrors were placed in a wind tunnel and abraded by windblown particles of quartz; in both cases, the wind speed was just above threshold, but because of the low atmospheric density on Mars, the wind speed is greater than on Earth to accomplish the same particle movement. The mirror in the martian case (a) is more severely abraded than the Earth case (b), primarily from the more energetic impacts resulting from the higher velocity. Area shown in both cases is about 500 μm by 750 μm.

about 16 times higher than in the Earth case. Both mirrors were then examined microscopically to assess the relative damage. The mirror that was abraded in the martian environment was much more severely damaged than the one abraded in the Earth environment, a result of the greater kinetic energies of the windblown sand grains on Mars. Thus, at

least qualitatively, higher rates of wind abrasion might be expected on Mars if aeolian materials and wind frequencies of threshold strength are comparable to Earth.

The Viking mission to Mars (1976-1981) returned additional evidence of extensive aeolian activity, including images of a sand sea equal in size to the largest erg on Earth (Tsoar et al., 1979) and views of the martian surface (Fig. 5) showing drifts of aeolian sediments (Mutch et al., 1976). However, the Viking results have also caused a reassessment of aeolian abrasion on Mars (Williams, 1981; Greeley et al., 1982). The pictures returned from the Viking landers show numerous surface rocks, none showing extensive aeolian modification. Viking Orbiter pictures reveal surfaces that have abundant small (~10 m) impact craters, the presence of which indicates surface ages that are millions or even hundreds of millions of years, but have been little modified by erosion or deposition of any type (Arvidson et al., 1979). If the wind erosion rates predicted prior to the Viking mission were correct, then these surface rocks and craters should have been obliterated long ago. Thus, there is a conflict between the predicted high rate of aeolian abrasion on Mars and the apparent constraints posed by the Viking results.

1.2 APPROACH

Ideally, all of the parameters involved in wind erosion on Earth and Mars would be observed and measured *in situ*. However, even if a field experiment were designed to obtain complete wind and particle flux data, it would be very difficult to separate the effects of the wind from other erosive agents such as water. Field measurements on Mars would be even more difficult and must await a future mission with an appropriately designed experiment.

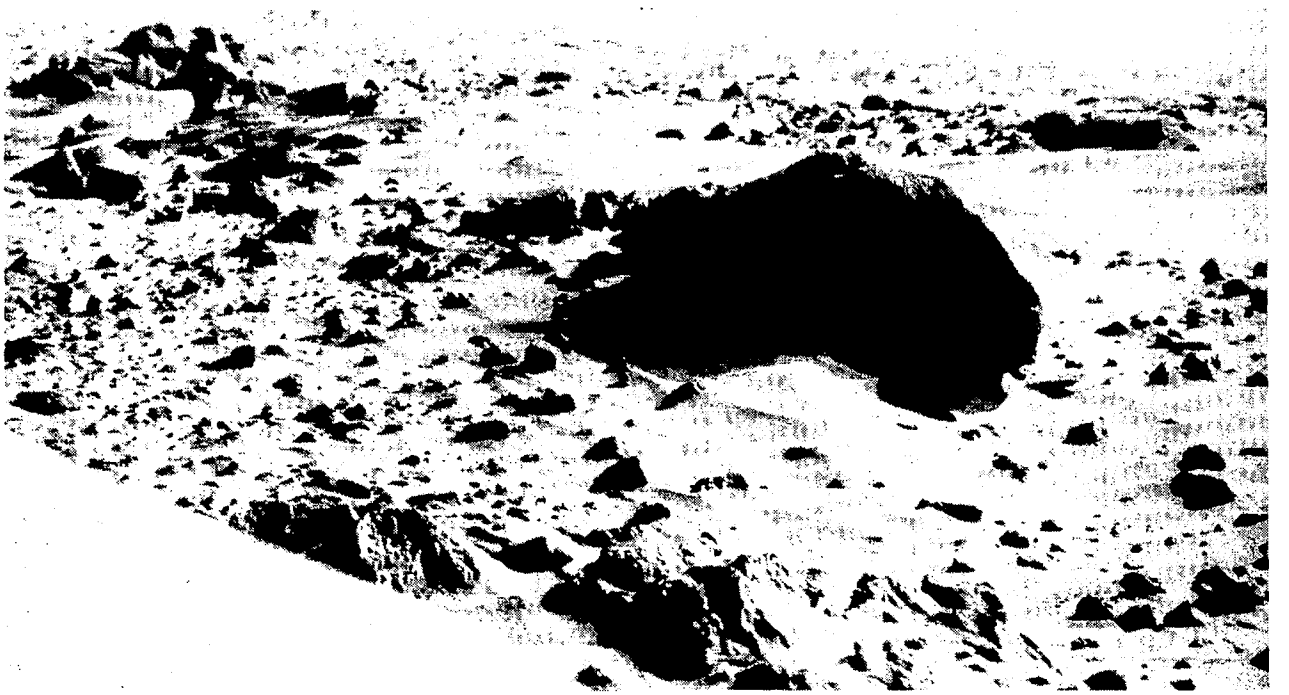

Figure 5. The surface of Mars as viewed from Viking Lander 1 in the Chryse Planitia region, showing a 2 m boulder, nick-named 'Big Joe,' numerous smaller rocks, and light-toned drifts of material interpreted to be aeolian deposits modified by wind erosion.

The approach in this investigation was to use results from laboratory simulations, supplemented by field experiments and theoretical considerations, in order to derive empirical results and calculated values for the factors required in estimating aeolian abrasion rates. Laboratory experiments have the advantage that conditions can be controlled and the parameters, such as particle velocity, can be isolated and studied separately. Furthermore, the atmospheric environment can be simulated to derive data appropriate for Mars.

1.3 ORGANIZATION

We present our results in six sections. The introduction is followed by a section describing the rocks, materials, and windblown particles used in our experiments and giving the rationale for their selection. The next three sections present results on the dynamics of windblown particles, susceptibilities to abrasion of the test materials, and wind frequency data. The last section gives estimates of aeolian abrasion rates on Earth and Mars and discusses the results.

2. EXPERIMENTAL MATERIALS AND RATIONALE FOR THEIR SELECTION

In this section we discuss the rocks and other materials used in our experiments to determine susceptibilities to abrasion appropriate for geological studies on Earth and Mars. We also consider the common sources of windblown particles and describe their characteristics in terms of aeolian abrasion.

2.1 TARGET MATERIALS

Eight materials (Table 2) were selected for abrasion experiments to represent a wide range of potential targets on Earth and Mars. The materials selected have a sufficiently wide range of textures and compositions to represent most rock types on Earth. Although there is relatively little information on martian rock types, the samples within the suite selected are probably appropriate for Mars. Data from the Viking lander inorganic chemistry experiments (Toulmin et al., 1977) suggest mafic to ultra-mafic compositions, probably involving basaltic rocks and their weathering products such as various montmorillonitic clays. Spectral data from remote sensing also suggest that large parts of the martian surface involve mafic and ultra-mafic materials (Singer et al., 1979). These data on the composition, combined with photogeological mapping, suggest that more than half of the surface of Mars is of volcanic origin (Greeley and Spudis, 1981) and provide the basis for selecting a large suite of volcanic rocks for the abrasion tests.

In addition to volcanic materials, substantial parts of Mars also appear to be mantled with sediments (Scott and Carr, 1978) which appear to range in thickness from less than 1 m to perhaps hundreds of meters. The degree of induration appears to be variable, including very friable duricrust sediments observed at the Viking landing sites and thick, apparently highly indurated deposits observed in the walls of the 'Grand Canyon' of Mars, *Vallis Marineris* (Carr, 1981). Possible origins of the various mantling deposits include windblown sediments, fluvial deposits, glacial deposits, and others. Thus, there appear to be fine-grained to glassy volcanic rocks on Mars, plus fine-grained pyroclastic materials and possible sedimentary clastic deposits ranging from breccias (generated partly from impact cratering) and conglomerates to clays.

2.2 WINDBLOWN PARTICLES

Most wind-transported particles on Earth range in size from ~micrometers ('dust') to several millimeters in diameter (Bagnold, 1941). Given the similar shape in the threshold curve (Fig. 3) it is likely that windblown particles on Mars would be of comparable size. Furthermore, most rock abrasion on Earth is apparently accomplished by sand-size (~60 to 2000 μm in diameter) grains transported in saltation, although finer material (Whitney and Dietrich, 1973) and perhaps even wind alone can be responsible for shaping ventifacts (Whitney, 1979). Sand-size particles result from primary sources such as volcanism and from various processes including weathering and fragmentation from impact cratering (Pettijohn et al., 1972). On Earth, most sand is quartz derived from the weathering of granite. Moreover, most aeolian sand has gone through some part of the hydrologic cycle, such as beach sand that is transported by the wind to form coastal dunes, or windblown desert sands derived

TABLE 2. Materials used in determining susceptibilities

MATERIALS	SOURCE	DESCRIPTION
Basalt	Amboy lava flow, California	Typical basalt in thin section. Contains euhedral plagioclase crystals that show some zoning. Crystal size is 0.5 - 1 mm. Glassy groundmass with some alteration.
Obsidian	Lookout Mountain, Long Valley Caldera, Mono Lake, California	In thin section the obsidian is almost totally glass. Contains some very small crystals and shows flow texture.
Tuff, welded	Bishop Tuff, Owens River Gorge near Bishop, California	The matrix shows both flow and compaction features. Contains elongated and somewhat devitrified pumice fragments. Has glass shards in matrix. Euhedral sanidine crystals of 1.5 - 2 mm diameter. Contains a small amount of quartz.
Tuff	Bishop Tuff, Owens River Gorge near Bishop, California	Contains some large pumice fragments. Matrix has glass shards but no evidence of flow or compaction. Euhedral sanidine crystals of 1.5 - 2 mm diameter.
Rhyolite	San Carlos Indian Reservation, Arizona	Granular texture with all crystals smaller than 1 mm. Contains microcline phenocrysts with a few quartz crystals and some accessory biotite and garnet.
Granite	Unknown	Coarse grained (up to 5 mm) granite. Primarily quartz and microcline, with some plagioclase and thin biotite crystals and accessory zircon.
Brick	Common red clay	In hand specimen, the brick is primarily red clay with some quartz and feldspar crystals, ranging in size up to approximately 2 mm.
Hydrocal	Common gypsum cement building material	In hand specimen, the hydrocal is uniform chalky mass, with no visible crystals or inhomogeneities, apart from an occasional vesicle.

from alluvium. Quartz is the common composition of aeolian sands, apparently because it is chemically stable and mechanically resistant and therefore is able to sustain repeated cycles of weathering and transportation. Because it is dominant in aeolian processes on Earth, quartz was selected as one of the primary agents of abrasion in our experiments.

Granite appears to be absent or rare on Mars and consequently there may be very

little quartz sand present (Smalley and Krinsley, 1979). Furthermore, under the present martian climate, and with the apparent lack of active volcanism and tectonism (Carr, 1981) and the present-day low rate of impact cratering, the generation of sand-size particles on Mars is probably suppressed in comparison to Earth. Nevertheless, the presence of sand dunes (Cutts, 1973; Cutts and Smith, 1973), some of which may be active (Tsoar et al., 1979), and other aeolian features (Sagan, 1973; Binder et al., 1977) suggest the presence of both sand-size particles and winds capable of transporting them. Remote sensing data for areas of aeolian activity on Mars and analyses of thermal inertia measurements also suggest the presence of sand-size particles (Peterfreund, 1981) as do analyses of materials at the Viking Landers (Moore and others, 1977).

Most martian dunes are very dark, including those of the large erg in the north polar region, and it has been suggested that they are composed of basalt particles derived from nearby volcanic plains (Tsoar et al., 1979). Thus, sand-size grains of basaltic compositions were used in many of our abrasion experiments to simulate Mars.

Because of the high wind speeds needed for sand entrainment on Mars, it has been suggested that sand-size particles would be very short-lived; the term 'kamikaze' (meaning divine wind in Japanese) grains was coined by Sagan et al. (1977) to describe particles that smashed against rocks and each other, forming fine-grained dust. Estimated particle sizes in the martian dust clouds is a few μm and smaller (Pollack et al., 1979b) and the kamikaze effect may be the principal mechanism to produce the dust. In addition, salt weathering, mechanical fracturing caused by the growth of salt crystals, has been shown to be important in the production of fine grains on Earth (Goudie et al., 1979) and may be an important process on Mars (Malin, 1974).

Laboratory experiments simulating the comminution of windblown sand on Mars give support to the idea of the kamikaze effect (Greeley, 1979). Experiments also show that windblown sediments generate electrical charges, a result confirmed by field observations on Earth (Mills, 1977). Both the magnitude of the charge and the polarity (positive or negative) appear to be functions of particle size, composition, impact velocity, and atmospheric density. Furthermore, the experiments showed that the dust generated from the breakup of the kamikaze grains clumped together, forming aggregates. These aggregates grew to diameters greater than several mm (Greeley, 1979). Evidently, differences in electrical charges among the dust particles were sufficient for aggregate formation. Because the electrical effects are enhanced in the rarified martian atmospheric environment, Greeley and Leach (1978) and Greeley (1979) suggested that *aggregates* may be an important part of the aeolian regime on Mars.

Windblown aggregates also occur on Earth. Some are generated during volcanic eruptions (Krinsley et al., 1980) and apparently are bonded by electrostatic charges. Most aeolian aggregates, however, are associated with playa deposits. Silt and clay playa deposits are often slightly indurated and/or cemented with various salts. During wind storms, sedimentary accumulations that are fragmented by dessication are picked up by the wind, rounded into sand-size grains and deposited in typical sand bedforms, including dunes (Huffman and Price, 1949; and others).

Sand-size aggregates of fine grains may be an important part of aeolian processes on Mars, and are known to occur on Earth. Thus, aggregates were used in some of our abrasion experiments for comparison with results using crystalline quartz and basalt sand grains.

2.3 SUMMARY

Windblown particles and rock targets of a wide range were selected for study in our experiments to simulate aeolian abrasion on Earth and Mars. Potential rock targets include igneous and sedimentary rocks which are common on Earth. Experiments involving basaltic rocks were emphasized for Mars, as basalts appear to be common on the Red Planet. Three types of particles – quartz, basalt, and aggregates of fine grains – were used as the abrading particles.

3. DYNAMICS OF WINDBLOWN PARTICLES

Of the three parameters required to determine the rates of wind abrasion, the one dealing with the dynamical characteristics of windblown particles is the most complicated and difficult to assess. For any given wind, the saltation flux and trajectories of windblown particles vary with surface roughness, height above the surface, and atmospheric density. Thus, in order to consider wind erosion on Earth and Mars for times in the past when the climate and atmosphere might have been different, these characteristics must also be known for a range of atmospheric densities.

3.1 METHODOLOGY

Our approach was to run wind tunnel experiments to determine as many of the particle characteristics as possible for Earth conditions, then to repeat the experiments under simulated martian conditions. Some of the results for the terrestrial cases were compared with results from field experiments in order to verify the wind tunnel simulations and to provide a basis for extrapolation to Mars. Because not all conditions for Earth or Mars could be satisfied in laboratory simulation, numerical models were derived based on a combination of theory and experiments to allow calculations of flux and saltation trajectories for a wide range of conditions.

Wind Tunnel Experiments

Experiments were performed in an open-circuit wind tunnel (Fig. 6) using particle

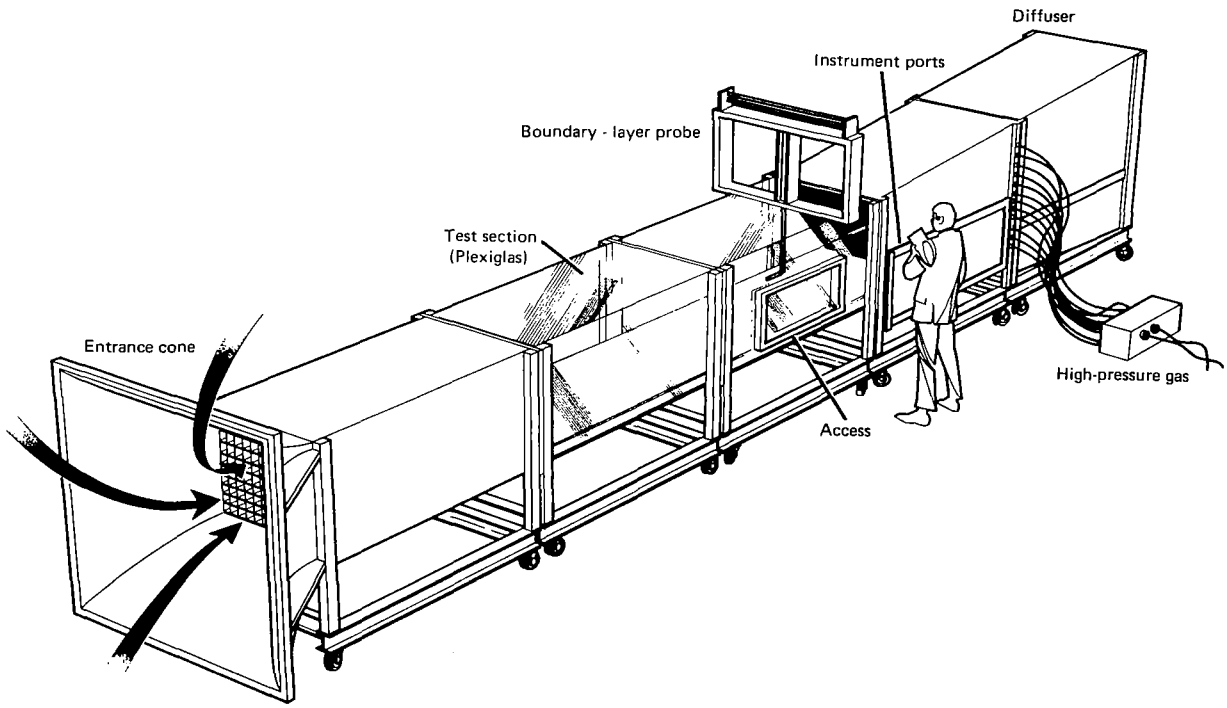

Figure 6. Diagram of the Martian Surface Wind Tunnel (MARSWIT). MARSWIT is an open-circuit, atmospheric boundary layer tunnel 14 m long, with a 1.1 m^2 test section. The tunnel is housed in an environmental chamber in which the atmospheric pressure can be varied from 1 bar to about 3 mb for martian simulations; at low pressures, carbon dioxide is used as the atmosphere, appropriate for Mars.

collectors to determine particle flux and instruments to determine particle velocity. An experimental matrix was developed combining atmospheric pressure, particle diameter, freestream wind velocity, and height above the surface (Appendix 1). Atmospheric pressures of 1 bar (Earth case) and an average of ~7 mb (Mars case) were used. Three particle sizes were selected for analyses: 715 μm, representing coarse sand, 350 μm for typical dune sand, and 92 μm, the size most easily moved by lowest strength winds (Fig. 3).

For both the Earth and Mars experiments a wide range of freestream wind velocities was selected, including high speeds to simulate storm conditions when substantial aeolian abrasion probably occurs. Crushed and sieved walnut shells were used in experiments to simulate Mars. Their lower density helps to offset the differences in gravity between Earth and Mars, as discussed below. Quartz sand was used in terrestrial experiments.

Particle collectors (Fig. 7) were used to determine flux as a function of height above the surface. Each collector was a wedge-shaped box, open at the upwind end to sample a cross sectional area of 2.4 cm^2 perpendicular to the flow direction. The larger, downwind end was covered with 40 μm mesh. A small baffle was placed in the collector to prevent particles from bouncing out of the front end or damaging the screen. The design used here was developed to maximize the collection of the particles with minimum interference of the air flow, although no particle collector is 100% efficient.

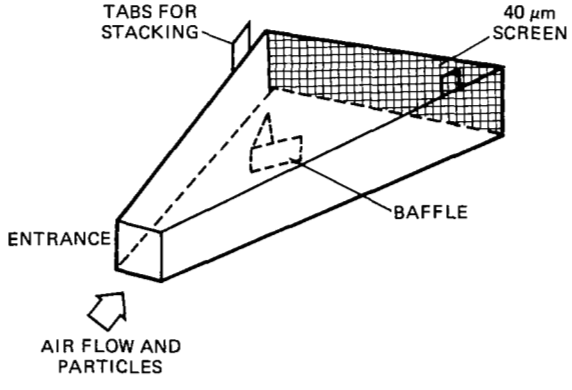

Figure 7. Diagram of particle collector used to determine flux. Collector is made of plexiglass; wind tunnel smoke tests were carried out to determine optimum angle for the wedge which would allow maximum efficiency for particle collection with minimum interference to air flow. Baffle prevents particles from bouncing back out the front or damaging the screen. Tabs on the side enable collectors to be stacked.

Particle flux (q) as a function of height above the surface was determined as the mass of particles caught per unit area of the collector per unit time. Although the collectors could be stacked to sample the entire cross section of the wind tunnel from the floor to the ceiling, preliminary tests showed erratic particle distribution at heights above 65 cm, evidently as a result of particles bouncing from the ceiling. Because of this behavior and because very few particles occur at these heights, collection in most experiments was made from the surface to 65 cm above the surface. Total particle flux, Q, was determined by summing the masses caught in the individual collectors.

Particle speed was determined with a velocimeter (Schmidt, 1977). The velocimeter produces a light beam perpendicular to the wind stream, focused on two light-sensitive semiconductors that detect the shadow of any particle as it crosses two separate portions of the light beam (Fig. 8). Parallel windows limit the field of view of the light receivers; an electronic unit connects the two phototransistors such that a particle passing through the light beam produces a positive voltage pulse as it shadows the first window, and a negative pulse at the second window. To determine particle speed the time interval between positive and negative pulses is measured with an oscilloscope. This time interval, in conjunction with the known separation of the sensor windows, enables the particle velocity to be

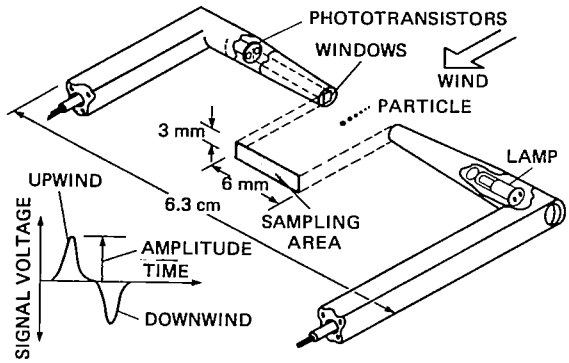

Figure 8. Schematic diagram of particle velocimeter; device consists of a light source and two phototransistors; as a particle passes through the beam, the upwind phototransister registers a positive voltage, then the second (downwind) phototransister registers a negative voltage; the difference between the two signals yields time (hence velocity); the amplitude is a function of grain size (from Greeley et al., 1982).

determined. About two hundred data points were obtained for each run. To investigate rates of rock abrasion corresponding to various heights above the surface, particle velocities were measured at various heights above the wind tunnel floor.

High speed 16 mm motion pictures were taken for some of the Earth-case wind tunnel experiments to determine saltation trajectories and to validate the velocities determined with the velocimeter (Greeley et al., 1982, 1983). The camera was positioned perpendicular to the particle flow and recorded the saltation cloud at 2,000 to 10,000 frames per second. The films were studied with a Vanguard Motion Analyzer using film timing marks at 0.001-second intervals recorded during the experiment.

Field Experiment

A field experiment was conducted to provide a calibration of the wind tunnel results under natural aeolian conditions using the same techniques and instruments as employed in the laboratory. The field site was located at Waddell Creek State Beach, about 100 km south of San Francisco. The beach consists of wind-transported marine sands and was readily accessible to equipment required for the experiment. In November 1981, a Hycam 16 mm motion picture camera was installed to record saltating particles at framing rates up to 8000 frames per second. Concurrent measurements of wind velocity were made 1 m above the surface. Particle collectors were placed in the wind stream to determine particle flux. Seven successful experiments were conducted for wind speeds ranging from about 4.5 to 7.0 m/sec.

3.2 PARTICLE VELOCITY

Most windblown particles near the ground are transported in saltation. The path that a saltating grain follows is called the saltation trajectory (Fig. 9). The velocity of the grain generally increases throughout its trajectory, although by the time it has reached maximum height above the ground, most grains will have achieved about 50% of their maximum velocity. For most of their trajectory, saltating particles travel at some fraction of the free-stream wind speed. Because meteorological data provide only wind speeds (not particle velocities) it is necessary to know particle

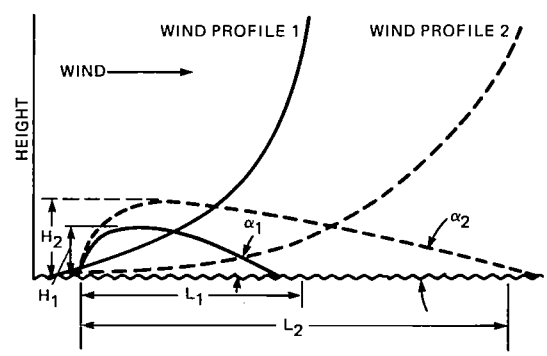

Figure 9. Diagram showing two typical saltation trajectories; solid path corresponds to low wind speed (profile 1) and has low (H_1) and short path (L_1) in comparison to path of particle driven by high wind speed (profile 2).

velocity as a function of wind speed in order to calculate rates of abrasion. Furthermore, at any given instant and at any given place within the saltation cloud there is a complex spectrum of particle paths and speeds. Thus, it is also necessary to know the velocity distributions of particles as functions of grain size, wind speeds, and heights above the ground.

Figure 10 shows typical velocity distribution within saltation clouds in terrestrial simulations, measured at a single height above the floor of the wind tunnel. Velocities are given in m/s and as percentages of the freestream wind velocity. In general, particles travelling at greater heights are also travelling at higher speeds. Evidently, this is a reflection of the increase in wind speed with height

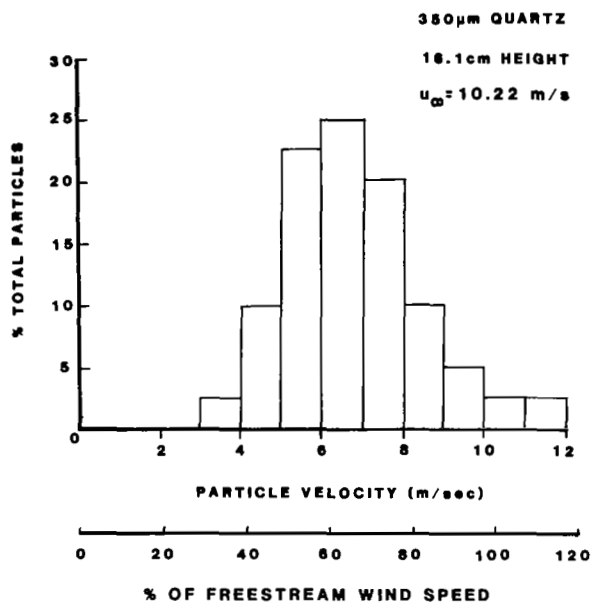

Figure 10. Distribution of particle velocities at a height of 16.1 cm above the surface for 350 μm diameter quartz grains subjected to a freestream wind speed of ~10.22 m/s in a simulation of Earth (u_* ≈ 0.6 m/s). The velocity distribution is typical and can be expressed as a mean value with an associated one standard deviation range about the mean, as shown. Later figures will present only the mean and range (from Greeley et al., 1983).

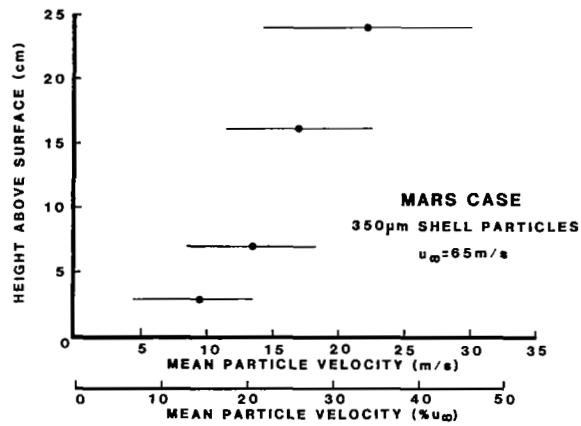

Figure 11. Particle velocities for four different heights above the surface for 350 μm walnut shell particles subjected to a freestream wind speed of 65 m/s (u_* = 3.4 m/s) in a low atmospheric pressure (6.6 mb) to simulate the martian environment (from Greeley et al., 1983).

above the ground, through the turbulent boundary layer. In addition, because particles at greater heights tend to have longer saltation trajectories, there is a longer interval of time for them to be accelerated by the wind. Note also that some grains travel at velocities exceeding the wind speed, which probably results from elastic rebound of grains in saltation. Figure 11 shows similar results obtained in experiments simulating Mars.

Figure 12 compares velocity data for particles on Earth with those of Mars under similar dynamic conditions for both low and high wind speeds. 'Low' refers to speeds about 25% greater than threshold; 'high' refers to storm conditions, where winds are about twice threshold. In all cases, particles travel at a higher percentage of the freestream wind speed on Earth than on Mars. This suggests a more efficient coupling of the particles with the wind in the denser terrestrial atmosphere. Because wind speeds are about an order of magnitude higher on Mars for particle motion, the grains would have to be accelerated to a much greater speed on

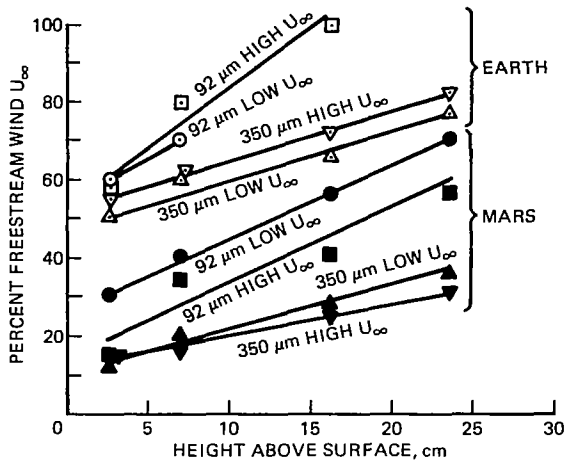

Figure 12. Average velocity of particles 350 and 92 μm in diameter as a function of height above surface at 10^3 mb pressure (Earth case) and 6.5 mb pressure (Mars case); both cases are run at freestream wind speeds just above threshold ('low' u_∞) and for storm conditions ('high' u_∞).

Mars in comparison to Earth in order to reach the same percentage of the freestream. Even though the saltation trajectory is longer on Mars, they may not be in flight long enough for an acceleration comparable to Earth. However, the lower percentage could also result partly from experimental error. The saltation path length on Mars is longer than on Earth (discussed below) and in the wind tunnel the saltation cloud in martian simulations may not become fully developed because of the limited wind tunnel length.

3.3 SALTATION MODEL

A computational model of particle saltation was developed in order to determine velocities and trajectories of particles for a wider range of conditions than could be simulated in the laboratory. In the model, a one-dimensional flow regime is assumed for calculations of the trajectories. The velocity in the vertical (y) direction is zero and the velocity, u, in the flux (x) direction is a function of height above the surface. A viscous sublayer develops in the wind flow when the wind speed is below threshold (White et al., 1976). However, when minimum threshold speeds (u_{*t}) are reached, the optimum-size particles (Fig. 3) begin to saltate, which causes the viscous sublayer to degenerate and form a fully turbulent boundary layer.

Our computational model of saltation trajectories is based on the equations of motion of a single particle (White and Schulz, 1977; Fig. 13):

$$m_p\ddot{x} = L\frac{\dot{y}}{v_r} - D\frac{\dot{x} - u}{v_r} \qquad (2)$$

$$m_p\ddot{y} = -L\frac{\dot{x} - u}{v_r} - D\frac{\dot{y}}{v_r} - m_p g \qquad (3)$$

where m_p is the particle mass, u is the wind velocity, $(\dot{x}, \dot{y})$ are the particle's horizontal and vertical velocity, $(\ddot{x}, \ddot{y})$ are the particle's horizontal and vertical acceleration, and v_r is the velocity of the particle relative to the velocity of the wind and is equal to $[(\dot{x} - u)^2 + \dot{y}^2]^{1/2}$. Aerodynamic force on a particle is proportional to its cross-sectional area, A, times the difference in pressure, Δp, across the particle. Bernoulli's equation states

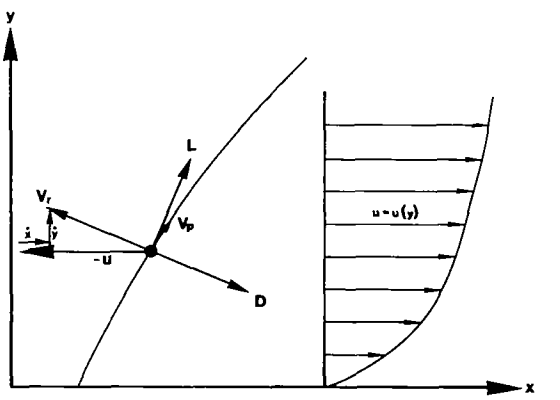

Figure 13. Force diagram for a saltating particle. L denotes lift force; D, drag force; v_p is the instantaneous particle velocity and v_r is the velocity of the particle relative to the wind velocity (modified from White and Schulz, 1977).

$$\Delta p = (1/2\ \rho_a v^2) \quad (4)$$

where ρ_a is the atmospheric density and v is the air velocity. Hence

$$L \propto 1/2\ A\ \rho_a\ v_r^2 \quad (5)$$

$$D \propto 1/2\ A\ \rho_a\ v_r^2 \quad (6)$$

Assuming the particles are spherical and of uniform density, we can write

$$L = 1/8\ C_L\ \rho_a\ \pi\ D_p^2\ v_r^2 \quad (7)$$

$$D = 1/8\ C_D\ \rho_a\ \pi\ D_p^2\ v_r^2 \quad (8)$$

where C_L is the coefficient of lift, C_D is the coefficient of drag, and D_p is the particle diameter. We can now substitute (7) and (8) into (2) and (3) and rearrange

$$\ddot{x} = -3/4\ \frac{\rho_a}{\rho_p}\ \frac{v_r}{D_p}\ [C_D\ (\dot{x} - u) - C_L \dot{y}] \quad (9)$$

$$\ddot{y} = -3/4\ \frac{\rho_a}{\rho_p}\ \frac{v_r}{D_p}\ [C_D \dot{y} + C_L\ (\dot{x} - u)] - g \quad (10)$$

The drag coefficient of a sphere is strongly dependent upon the Reynold's number. The empirical formulas of Morsi and Alexander (1972) are used for its determination in our numerical calculations. The initial conditions are the same as those used by White et al. (1976), in which the particle is at rest on the surface and, as the wind speed is increased above threshold, particles begin to move. For calculations in the martian atmosphere it is necessary to include the effects of slip flow caused by the low density atmosphere, although the slip flow factor only becomes significant for the smaller-size particles in the calculations (White, 1979).

Figure 14 displays typical computed particle trajectories for Earth and Mars when lift forces due to the Magnus effect (lift force produced by spin) are taken into account (White and Schulz, 1977). The percentage values at various positions along the trajectory are the ratio of particle speed to the free-stream wind speed. In general, the percentage of freestream wind speed that a particle reaches is about the same for all calculated particles at similar positions in their trajectories. Particles accelerate to nearly half of the freestream wind speed in the initial lifting phase of their trajectories, which corresponds to about 1/4 of their path length, L. Note, however, that particles more nearly approach freestream wind speed on Earth than they do on Mars, similar to the results determined experimentally.

3.4 PARTICLE FLUX

Numerous investigators have analyzed mass transport, both from experimental and theoretical approaches. Bagnold (1941), for example, carried out experiments to determine Q and then considered the flux in terms of momentum loss of the air due to sand in saltation. Sharp (1964) collected grains within saltation clouds at various heights over long periods of time, then determined the total masses and particle size distributions; however, concurrent wind data are not available. Thus, in order to obtain data appropriate for both Earth and Mars, experiments were carried out and a numerical model was developed.

In our experiments, particles were placed in the wind tunnel upwind of an array of collectors (Fig. 15). The collectors have a remotely-operated trap door that can be opened and closed to sample the saltation cloud for a discrete interval of time. The wind speed was increased and held steady to produce a fully developed saltation cloud. The trap door was then opened to sample the saltating particles. At the conclusion of the run, particle masses were determined for each collector to obtain values of q for each height.

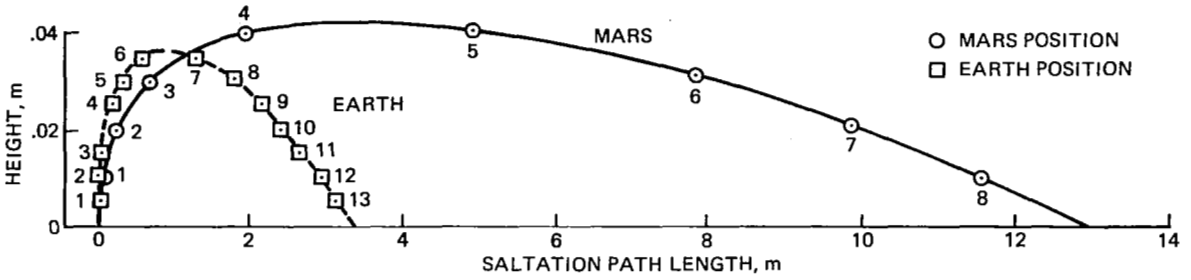

POSITION	EARTH VELOCITY, m/sec	EARTH PERCENT, V_∞	MARS VELOCITY, m/sec	MARS PERCENT, V_∞
1	2.6	10	5.3	5.3
2	4.7	18	12.9	12.9
3	7.2	28	22.6	22.6
4	12.6	49	37.3	37.3
5	15.4	60	53.2	53.2
6	18.8	73	61.8	61.8
7	22.1	90	65.7	65.7
8	23.1	90	67.6	67.6
9	23.5	91		
10	23.6	91		
11	23.7	92		
12	23.7	92		
13	23.5	91		

Figure 14. Calculated trajectory for grains in saltation on Earth and Mars for wind speeds about 25% above threshold, showing much longer trajectory for martian case. Positions along the trajectory show the instantaneous velocity (shown in both m/s and as a percentage of freestream wind speed) of the particle. Note that vertical scale is greatly exaggerated.

Figure 16 shows q as a function of height for 92 μm grains at three wind speeds in the wind tunnel compared to results obtained in the field experiment at Waddell Creek where the average grain size was about 300 μm. In general, there is an increase in flux closer to the surface, and at greater freestream velocities.

Figure 17 shows experimental results for Mars to determine q for 92 μm particles versus height for wind speeds ranging from 58 to 123 m/sec. In these and other martian simulations particles composed of walnut shells approximately one third the density of grains expected on Mars were used to compensate partly for the lower martian gravity (Greeley et al., 1977a). Although this technique is valid for threshold tests and for determining flux in terms of *numbers* of particles, the experimental data for flux *mass* must be adjusted (Greeley et al., 1982). Thus, in Figure 18 the gravity-adjusted data are shifted upwards by a factor of 2.6 (the density difference between walnut shells and particles expected on Mars, such as basalt). As in the terrestrial cases, there is a general decrease in particle flux with height above the surface. In addition there is an abrupt break in the flux at about 30 cm above the surface. This break may represent the transition from grains that are transported primarily in saltation near the surface to grains moving mostly in suspension at levels above 30 cm.

Total mass flux, Q, was determined by summing incremental flux, q, for the total column sampled. Figure 19 shows total flux,

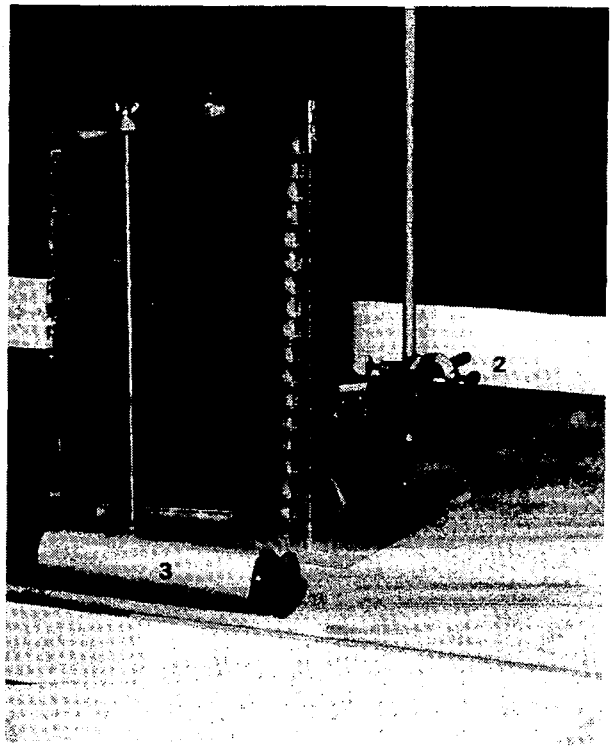

Figure 15. View of stacked particle collectors (1) used to determine flux of saltating grains. Samples are taken in intervals of 2 cm above the floor; trap door device allows precise timing of collection during fully-developed saltation cloud. Also shown is particle velocimeter (2) and electrometer probe (3) used to measure electrical current generated by wind-blown grains. Air flow is from right to left (from Greeley et al., 1982).

Q, for freestream wind tunnel speeds ranging from ~6 to 12.0 m/s for 92 μm quartz particles, simulating terrestrial conditions. Martian simulations are shown in Figure 20 which give total flux, Q, for freestream speeds ranging from about 55 to 90 m/s for 92 μm; both experimental and gravity adjusted data are shown. Few particles in suspension were counted. In general, there is an increase in flux with increasing wind velocity. Thus, flux is higher on Mars than on Earth for dynamically similar conditions (same $u*/u*_t$), because of the higher wind speeds required on Mars for particle entrainment.

Model for Calculation of Flux

An estimate of the total amount of surface material transported by the wind may be made by examining the physics of the process. The key parameter in estimating surface-material movement rates is the characteristic path length of saltating particles. Several investigators have developed both empirical and theoretical methods to calculate path lengths (Bagnold, 1941; Kawamura, 1951; Tsuchiya, 1969). Tsuchiya has a theoretical development based on successive saltating leaps. However, it is necessary to

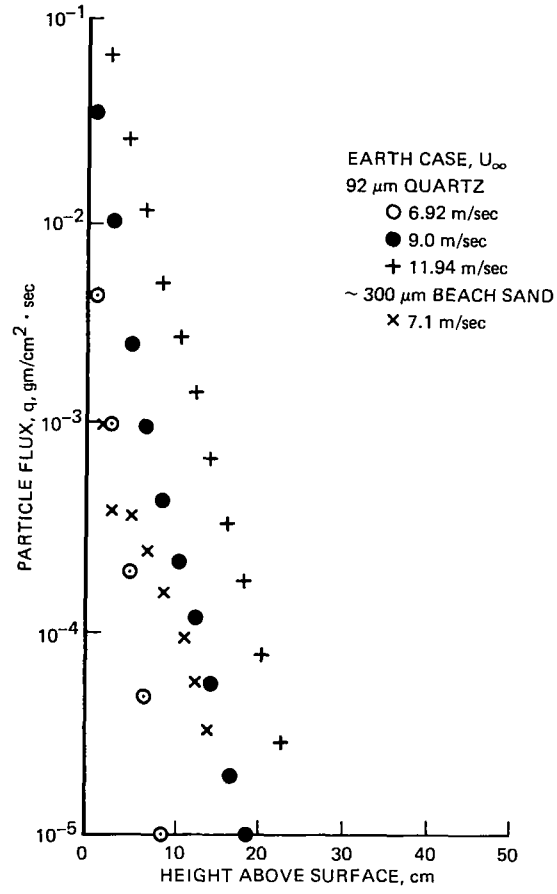

Figure 16. Particle flux, q, of 92 μm quartz grains as a function of height for three freestream winds (Earth case), showing general increase in flux with wind speed, and flux for 300 μm particles as determined from field experiment.

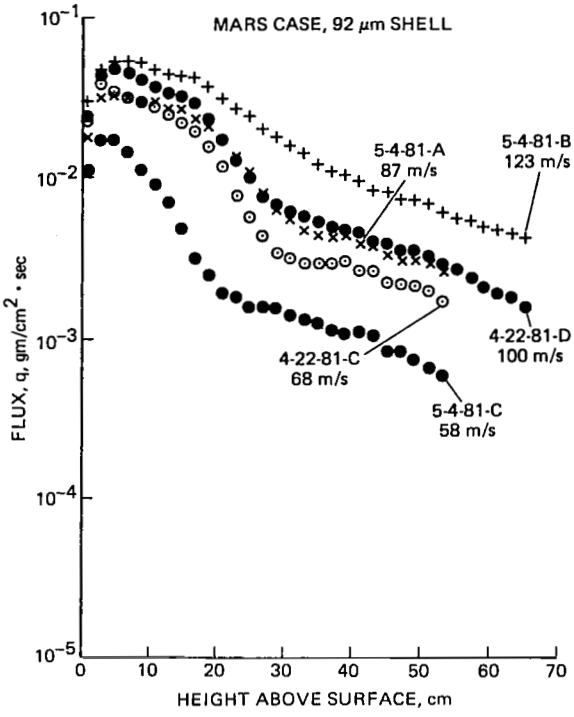

Figure 17. Particle flux, q, for 92 μm particles as a function of height for 5 wind speeds in the martian wind tunnel at ~6 mb atmospheric pressure.

know the initial or maximum vertical component of velocity at lift-off for the particle in order to calculate its path length. This component is generally a function of the flow conditions. Formulation of this type, with the path length a function of the vertical velocity, does not lend itself well to calculations of surface material movement. For our application it is useful to express the path length in relation to the threshold shear stress exerted on the surface by the wind, as presented by Kawamura (1951). The surface shear stress τ_o consists of two elements. The first is the ordinary wind shear, τ_w, caused by the motion of the wind flow over the surface. The second stress, τ_s, comes from the impact of particles colliding with the surface.

Kawamura found that τ_w increases with increasing wind friction speed, u_*, until u_{*t} is reached, then it remains approximately constant at a value of τ_t, hence,

$$\tau_o = \tau_s + \tau_w \tag{11}$$

or

$$\tau_s = \tau_o - \tau_w \tag{12}$$

Bagnold (1941) and Kawamura state that the stress on the surface caused by the impact of saltating grains is equal to the momentum lost by the grains:

$$\tau_s = G_o (u_f - u_i) \tag{13}$$

where G_o is the number of grains landing per unit area per unit time, u_f is the final grain speed at surface impact, and u_i is the initial grain speed at particle lift off.

It can be assumed (Kawamura, 1951) that there is a linear relationship between the particle momentum lost occurring in the horizontal and vertical directions

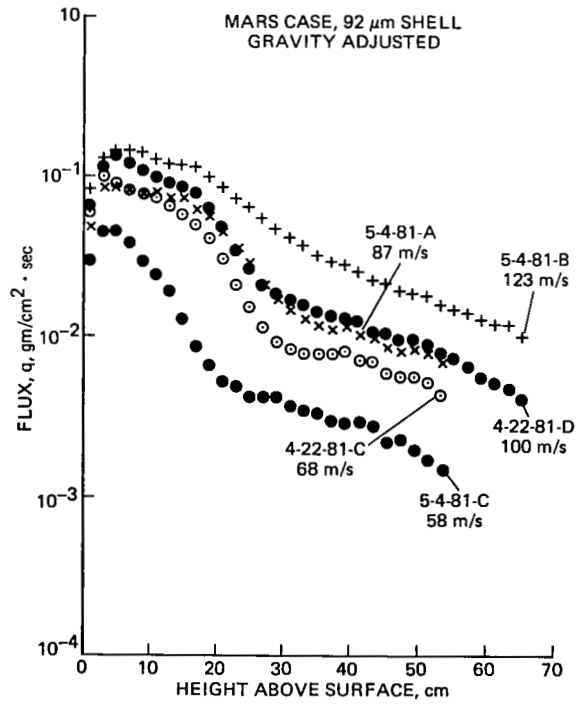

Figure 18. Same data as in Figure 17 corrected for martian gravity.

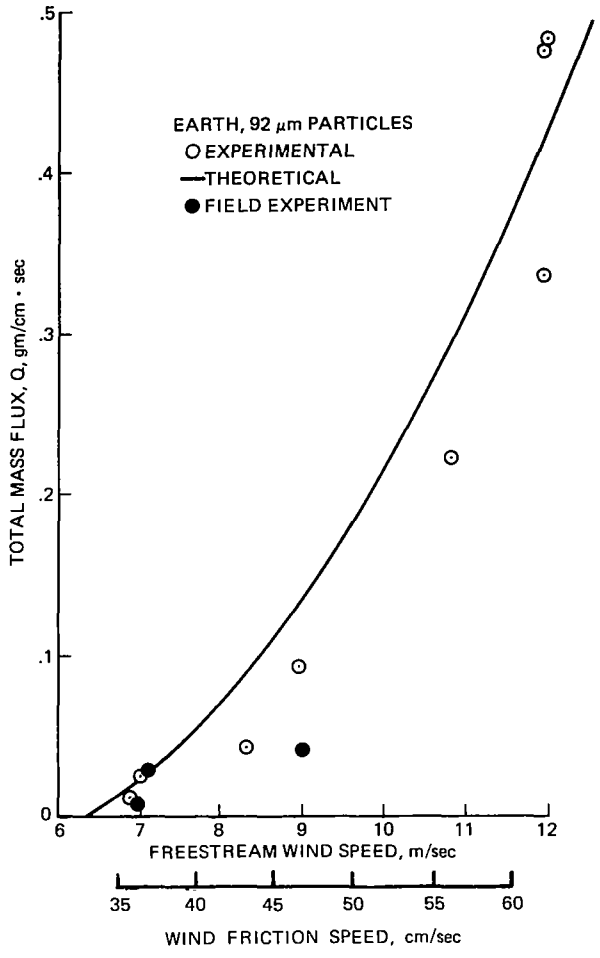

Figure 19. Particle flux, Q, as a function of free-stream wind speed, u_∞, for 92 μm quartz particles in Earth wind tunnel simulations compared with flux predicted by Equation 33.

$$G_o \overline{|u_f - u_i|} = \xi G_o \overline{|w_f - w_i|} \qquad (14)$$

where ξ is a constant, and u and w are the horizontal and vertical components of the particle velocity, v, respectively.

After the collision with the surface a bouncing particle traveling vertically with speed w_i will again return to the surface with the same speed $w_f = -w_i$ on the average. Hence

$$\overline{|(w_f - w_i)|} = 2 w_i \qquad (15)$$

Substituting (15) into (14) into (13) yields

$$\tau_s = 2 \xi G_o \overline{w}_i \qquad (16)$$

Substituting into (12)

$$2 \xi G_o \overline{w}_i = \tau_o - \tau_t \qquad (17)$$

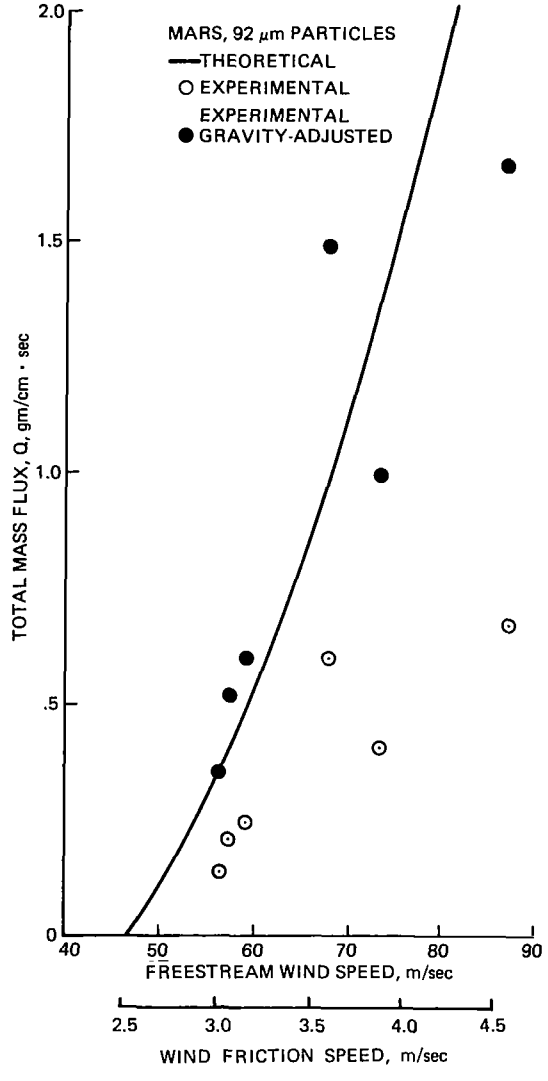

Figure 20. Particle flux, Q, for 92 μm particles in experiments, as adjusted for Mars gravity, and compared with flux predicted by Equation 33 (from Greeley et al., 1982).

From the definition of surface friction speed

$$u_* \equiv [\tau_o/\rho_a]^{1/2} \qquad (18)$$

where ρ_a is the atmospheric density, Equation (16) can be rewritten as

$$2\,\xi\,G_o\,\bar{w}_i = \rho_a\,(u_*^2 - u_{*t}^2) \qquad (19)$$

From field studies of saltation, Kawamura (1951) found that

$$G_o = K_1\,\rho_a\,(u_* - u_{*t}) \qquad (20)$$

which also agreed with numerical solutions of particle motion (White, 1979). Substituting (20) into (19) yields

$$2\,\xi\,K_1\,\rho_a\,(u_* - u_{*t})\,\bar{w}_i = \rho_a\,(u_*^2 - u_{*t}^2) \qquad (21)$$

We can solve (21) for $\bar{w}_i$, by rearranging and collecting the constants

$$\bar{w}_i = K_2\,(u_*^2 - u_{*t}^2)/(u_* - u_{*t}) = \bar{w}_i = K_2\,(u_* + u_{*t}) \qquad (22)$$

The average saltation path length, λ, can be calculated from this result in the following manner. From elementary physics we know that the time aloft for a particle with initial upward velocity, w_i, is

$$t = 2\,\bar{w}_i/g \qquad (23)$$

where t is time aloft and g is the acceleration due to gravity. During time t, the particle will be moving downstream with an average velocity $\bar{u}_i$. Applying basic physics equations of distance traveled, the saltation path length, L, is

$$L = \bar{u}_i\,t \qquad (24)$$

Substituting (23) into (24):

$$L = 2\frac{\bar{u}_i\bar{w}_i}{g} \qquad (25)$$

Because $\bar{u}_i \propto \bar{w}_i$ (from 14)

$$\lambda = 2\,K_3\,\frac{\bar{w}_i^2}{g} \qquad (26)$$

Substituting (22) into (26) and collecting constants

$$\lambda = K_4\,\frac{(u_* + u_{*t})^2}{g} \qquad (27)$$

We now have the necessary information to calculate a total saltation lane flux, Q. If we consider a zone with length λ, downwind of a unit width lane, no particle can possibly land in that zone without first passing over that lane width; also, no particle can pass over the lane width and fail to land in the zone. Hence

$$Q = G_o\,\lambda \qquad (28)$$

Thus, the amount of material passing over the lane width is equal to the amount of material landing on the surface per unit area times the length of the zone. We can substitute (20) and (27) into (28)

$$Q = K_1\,\rho_a(u_* - u_{*t})K_4\,\frac{(u_* - u_{*t})^2}{g} \qquad (29)$$

The final form of the theoretical total flux is

$$Q = K_5\,\frac{\rho_a}{g}(u_* - u_{*t})(u_* + u_{*t})^2 \qquad (30)$$

On Mars, there appear to be different interparticle forces as well as effects from changes in Reynolds number. These changes will alter the saltation characteristics by affecting the threshold friction speed. The flow field around individual particles (Knudsen and Reynolds numbers effects), shearing rate within the boundary layer, and the existence of a comparatively large (to Earth) viscous sublayer for nonsaltating flow will cause change in threshold values.

Using Equation 30, a comparison between Earth and Mars can be made

$$\frac{Q_E}{Q_M} = \frac{\rho_E (u_* - u_{*t})_M g_M (u_* + u_{*t})^2_E C_E}{\rho_M (u_* - u_{*t})_E g_E (u_* + u_{*t})^2_M C_M} \quad (31)$$

where the C's are constants of proportionality. Assuming that the ratio of friction speed to threshold friction speed, u_*/u_{*t}, is the same for both Earth and Mars (most areas on Earth are windier than Mars):

$$\frac{Q_E}{Q_M} = \frac{\rho_E g_M (u_{*t})^3_E C_E}{\rho_M g_E (u_{*t})^3_M C_M} \quad (32)$$

White (1979) has shown experimentally that under martian conditions substantially less stress is needed to move material than on Earth. This result supports the numerical results that show similar increases in particle path lengths on Mars and that the path length is almost directly related to the mass flux. Thus, it would be useful if Earth and Mars cases could be adequately described by a single universal equation. According to the analytical derivation, the only differences between the relations describing the two cases are the empirical constants C_E and C_M. If the constants of proportionality C_E and C_M are the same for both cases, this would indicate that the physics between the two tests remained unchanged, and would imply a universality to the mass flux process. As one would expect, the process of movement of surface material on Mars should be nearly the same as the process on Earth. Hence, the constants of proportionality between the two test cases should be nearly the same. From the wind tunnel data of both cases, a unitless empirical constant with a value of 2.61 was determined (White, 1979).

Figure 21 displays the mass flux versus a function of friction speeds. Here, both high- and low-pressure data collapse to a single line in support of the idea of a universal function describing the movement process. Hence, the following equation can be used in estimating mass flux on either Earth or Mars once the friction speed and threshold friction speed are known:

$$Q = 2.61 \frac{\rho_a}{g} (u_* - u_{*t})(u_* + u_{*t})^2 \quad (33)$$

The flux of material on Mars is consistently higher than on Earth, if the frequencies of winds above threshold are the same, in spite of the lower martian atmospheric density, due to: a) the higher u_{*t} required on Mars, b) the lower martian gravity and c) the typically longer saltation path lengths on Mars (discussed above). From Equation 32 the difference in Q between the Earth and Mars may be expressed as

$$Q_M = \frac{(u_{*t})^3_M \; Q_E}{(u_{*t})^3_E \; 13.5} \quad (34)$$

For example, the relationship between the material movement on Earth and on Mars, for equal ratios of u_*/u_{*t} of 1.47, would be Q_M/Q_E = 6, or 6 times as great on Mars for 200 μm particles. A direct estimate of flux

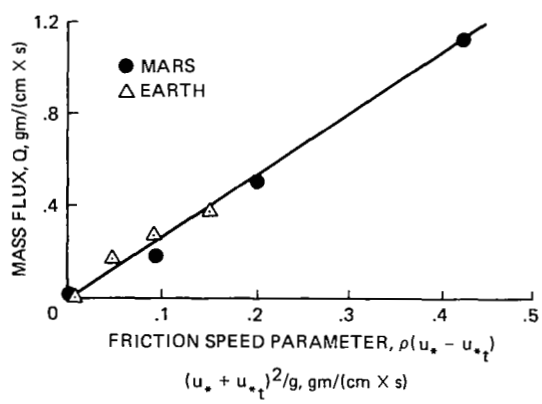

Figure 21. Particle flux, Q, as a function of friction speed parameter; one bar (Earth) and low pressure (Mars) data collapse to a single curve which is the straight line on the plot. Note the origin for both cases are data points, as they are used in determining the threshold friction speeds (from White, 1979).

rates on Mars can be made by employing the results shown in Figure 21. To obtain a numerical value, the threshold friction speed must be known. The value will vary with size of particles but, once known, a direct estimate of the mass flux can be made.

3.5 SUMMARY

In general, increases in freestream wind speed result in increases in the trajectory height and path length for grains in saltation, causing them to achieve higher velocities. This, in turn, results in higher rates of mass transport. Because of the higher wind speeds required for threshold on Mars, both particle velocities and fluxes are higher than on Earth, if the frequency of wind above threshold is the same. However, particle velocities seldom are greater than about 50% of freestream velocity on Mars, in contrast to Earth where particle velocities commonly meet and sometime exceed freestream velocity.

4. SUSCEPTIBILITY OF ROCKS TO AEOLIAN ABRASION

Rocks and minerals of different compositions and texture should have different resistances to abrasion by windblown particles. In this section we review previous studies of wind abrasion, discuss the mechanics of abrasion, and present the results of laboratory experiments that were conducted under controlled conditions in order to derive values that can be applied to estimates of abrasion on Earth and Mars.

4.1 PREVIOUS INVESTIGATIONS

Except for the work of Kuenen (1960), very few studies have been made to quantify aeolian erosion of natural materials, although ventifacts have been long recognized and described. Abrasion of metals, glasses, and ceramics is important in manufacturing and industrial processes. Much research has been done on the topic for engineering applications. The effects of target composition, impactor size and composition, and impact angle have been investigated experimentally (Neilson and Gilchrist, 1968; Sheldon and Finnie, 1966b). Experimental and theoretical studies of the mechanisms of material removal for both brittle and ductile materials were conducted by Adler (1976a, 1976b), Smeltzer et al. (1970), Sheldon and Finnie (1966a), Sheldon (1970) and Sheldon and Kanhere (1972) and a numerical prediction of abrasion on both ductile and brittle materials was made by Finnie (1960). The mechanism of abrasion of brittle fused silica was made by Adler (1974). The behavior of impacting particles during abrasion was studied by Tilly and Sage (1970). The initial and 'steady-state' erosion characteristics of a target in response to particle impact was noted by Tilley (1969) and discussed by Marshall (1979). Suzuki and Takahashi (1981) have conducted experiments of abrasion in a geological context.

4.2 THE MECHANICS OF ABRASION

The mechanisms by which aeolian particles disrupt and remove material in the abrasion process is not well understood. Discussion here is limited to aeolian abrasion of brittle materials (as opposed to ductile), appropriate for rocks and minerals, and is based primarily on interpretations of SEM photographs of materials abraded under laboratory conditions. Not all particle impacts lead directly to erosion; some may damage the surface but not necessarily remove material. Under most conditions material removal occurs where propagating fractures intersect.

Fracture Patterns Produced By Rounded Particles

Well-rounded particles such as sand grains impacting the flat surface of an elastic, brittle surface become flattened at the contact and the target surface is bent downwards. The area of contact increases with particle radius and applied load. If the load exceeds a critical limit, a circular crack – called a *Hertzian fracture* – develops around the indentation site, generally at a radius 10 to 30% greater than the contact radius (Johnson et al., 1973). In its ideal form, the crack extends a short distance vertically into the specimen before turning outward and propagating into a conical frustrum, the depth of which increases with increasing load.

Andrews (1931), Knight et al. (1977), and others have shown that the surface diameter of a Hertzian fracture (D_H) is constant and independent of the impacting grain

velocity, a result in agreement with theory for perfectly spherical impactors. However, for well-rounded, but irregularly-shaped particles, the mean diameter of a population of cracks increases with velocity (Marshall, 1979; Fig. 22a). Because the impacting grains were not perfect spheres, the targets were subject to indentation with a wide range of radii and at low impact velocities only the smaller radii (which concentrate the impact stresses) were capable of producing Hertzian fractures. At high impact velocities (v_p) both large and small radii were effective and mean crack diameter (D_H) increased with velocity. The relationship $D_H \propto v_p^{0.47}$ was derived by Finnie (1960), which in comparison to the relationship between maximum contact radius (a_m) and velocity ($a_m \propto v_p^{0.4}$), implies that the cracks formed at

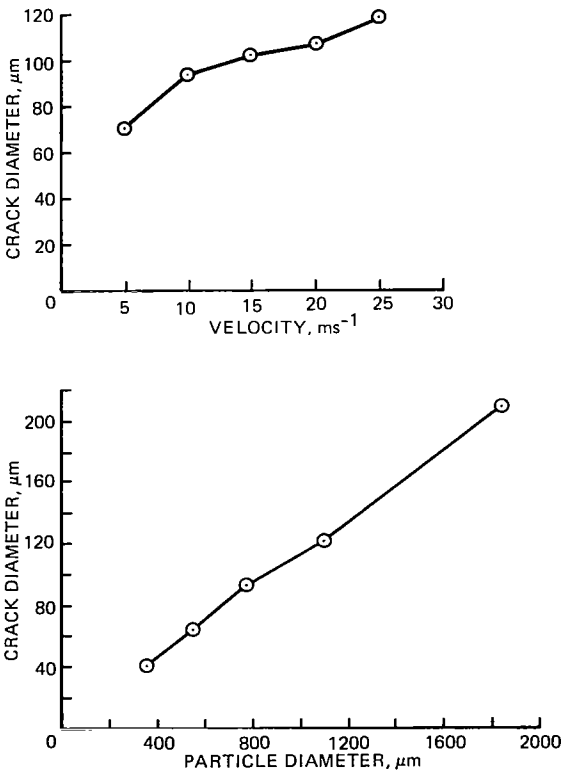

Figure 22. Effect of particle velocity (a, top diagram) and diameter (b, bottom diagram) on Hertzian – fracture diameter; each point represents the mean of 100 measurements of quartz grains impacting on quartz plates (after Marshall, 1979).

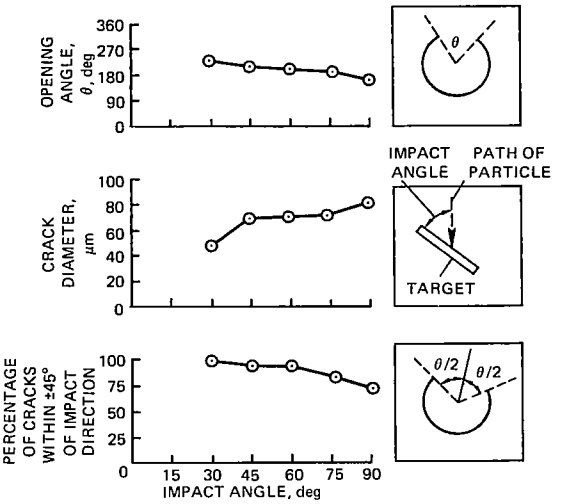

Figure 23. Effect of particle trajectory on opening angle, θ, defined in inset (a, top diagram), diameter (b, middle diagram) and orientation (c, bottom diagram) of Hertzian fractures. Each point represents the mean of 100 measurements (after Marshall, 1979).

about the time of pressure release. Johnson et al. (1973) observed cracks smaller than maximum contact size formed during unloading and attributed the behavior to an elastic mismatch between indentor and specimen which affects the stress field via frictional forces at the contact interface.

Figure 22b shows the effect of particle size (D_p) on the surface diameter of Hertzian fractures for impact of irregularly-shaped particles. Perfectly spherical indenters give rise to an exponential relationship of the form $D_H \propto D_p^{2/3}$ when $D_p < 7.0$ cm and a linear relationship when $D_p > 7.0$ cm (Tillett, 1956).

At impact angles less than 90° the tangential component of force introduced into the stress system inhibits cracking in front of the grain and the result is an arc-shaped or apparently incomplete Hertzian fracture (Fig. 23). As the angle decreases the opening angle θ increases (θ = the angle subtended by the 'horns' of the crack at an imaginary center of curvature of the arc), the diameter decreases, and the preferred orientation of the individual

crack – increases (orientation is defined as the direction pointed to by a line bisecting θ).

Fracture Patterns Produced By Angular Particles

Angular particles do not abrade in the same manner as rounded particles. A great diversity of erosion patterns can arise from only minor variations in particle shape and from the manner in which the particle strikes the surface. Lawn and Wilshaw (1975) consider the fracture propagation shown in Figure 24 to be a basic sequence during normal loading of a surface with a sharp point. Initial contact induces a zone of inelastic deformation (crushing and/or plastic deformation) and at some threshold stress initiates a vertical crack (or median vent) which propagates downward with increasing load. Upon unloading the median vent closes (but does not heal) and lateral vents develop which continue to propagate after removal of the impacting grain. Chipping can result if the lateral vents reach the surface of the indented specimen (Fig. 25). Often the median vent will break through to the surface of the specimen and give rise to a radial fracture trace. The length of the surface trace is an indication of the depth of the vent. For isotropic materials the number of median vents is limited only by the mutual stress-relieving

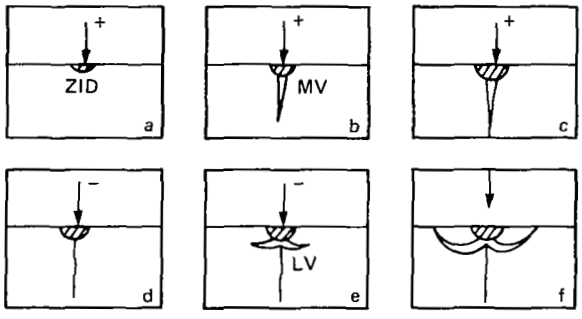

Figure 24. Crack propagation below a pointed particle; ZID is zone of inelastic deformation; MV is median vent; LV is lateral vent.

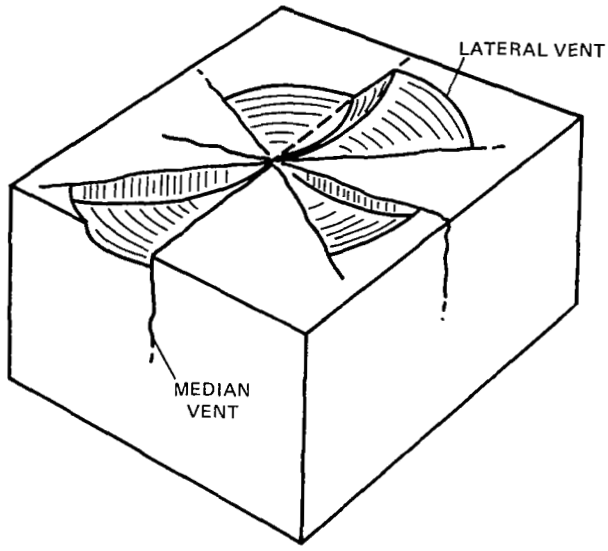

Figure 25. Surface pattern produced by intersection of lateral and median vents.

influence of neighbors; several intersecting the surface produce star-shaped patterns (Fig. 25). In anisotropic systems the vents tend to follow cleavage directions.

The Influence Of Fracture Patterns On Abrasion Rates

Abrasion rates of ventifacts reflect the stage of surface-texture evolution. For rounded particles impacting an initially smooth surface, textural development and related abrasion have the following evolution. During the embryonic phase of fracture network development, abrasion is inhibited (Fig. 26). At some critical spatial density of conical frustra, material becomes easily removed, but abrasion diminishes thereafter because the isolated frustra are difficult to remove. Impact on the top of a cone apparently only deepens the structure, whereas cone spacing prevents contact of rounded particles with surfaces between the cones. Abrasion on the final surface should be somewhat less rapid than during cone removal because surface roughness prohibits cone formation – such fractures probably have deeper penetration

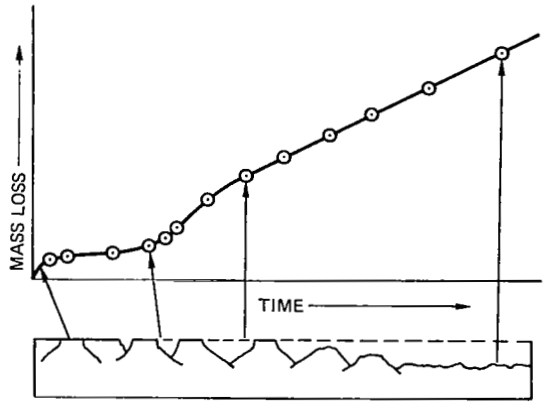

Figure 26. Mass lost in aeolian erosion as a function of time; profile in lower part of diagram is deduced from SEM observations of Marshall (1979), compared with laboratory experiments of Adler (1976b).

than cleavage-controlled chipping. Figure 27 shows scanning electron microscope photos of four evolutionary phases in this sequence; a, b, c and d correspond to the four stages signalled in Figure 26. Although this sequence of events is dependent upon the initial surface of the material, it may be typical for ventifacts if periods between abrasion permit chemical smoothing of the roughened abraded surface. For a ventifact impacted with angular particles, the textural development may proceed in the manner depicted in Figure 28.

4.3 ABRASION EXPERIMENTS

The susceptibility to abrasion (S_a) for different materials is expressed as the ratio of the material mass eroded to either the mass of impacting particles or the number of impacting particles. S_a varies with parameters such as impacting particle velocity (v_p) and angle of impact. Angle of impact is defined as the angle between the surface and the impacting particle and is the complement of the incidence angle.

In order to determine S_a values for various rocks under a wide range of conditions, an apparatus (Fig. 29) was fabricated that allows impact velocity, impact angle, impacting particle size and type, sample type, and atmospheric density and composition to be controlled (Appendix 2). Marshall (1979) found that anomalous weight losses occur in samples that were not pre-abraded and that have not attained a steady state in aeolian abrasion. Thus, all targets were pre-abraded prior to experiments to establish fracture patterns in their surfaces. Each target was weighed to ±0.1 mg before and after each run. Dust clinging to the target was removed by compressed air. The fraction of the total mass of particles impacting any target was determined from the total mass expended in the experiment by calculating the angle subtended by the target from the geometry of the apparatus and dividing by 360°. A check on the calculated impact mass was made by placing a particle catcher in the place of one of the sample stations.

Quartz sands were used as the abrading particles in most of the experiments because they are readily available, their behavior is fairly well understood, and nearly all previous abrasion experiments have involved quartz. However, basalt sands and sand-size aggregates of fine grains were also utilized in some experiments (Appendix 2).

Susceptibilities to abrasion were assessed in terms of five parameters: particle size, particle velocity, angle of particle impact, atmospheric density, and impacting particle composition.

S_a Versus Particle Diameter

Figure 30 shows S_a as a function of diameter of impacting particles (D_p = 75, 105, 140, and 160 μm) for basalt, obsidian, and hydrocal. Particles impacted at an angle of 90° at a velocity of 20 m/s in a CO_2 atmosphere of 5 mb pressure, conditions comparable to a martian environment. The effect of particle size in the range analyzed is fairly well defined by a slope of ~3 on a log-log plot

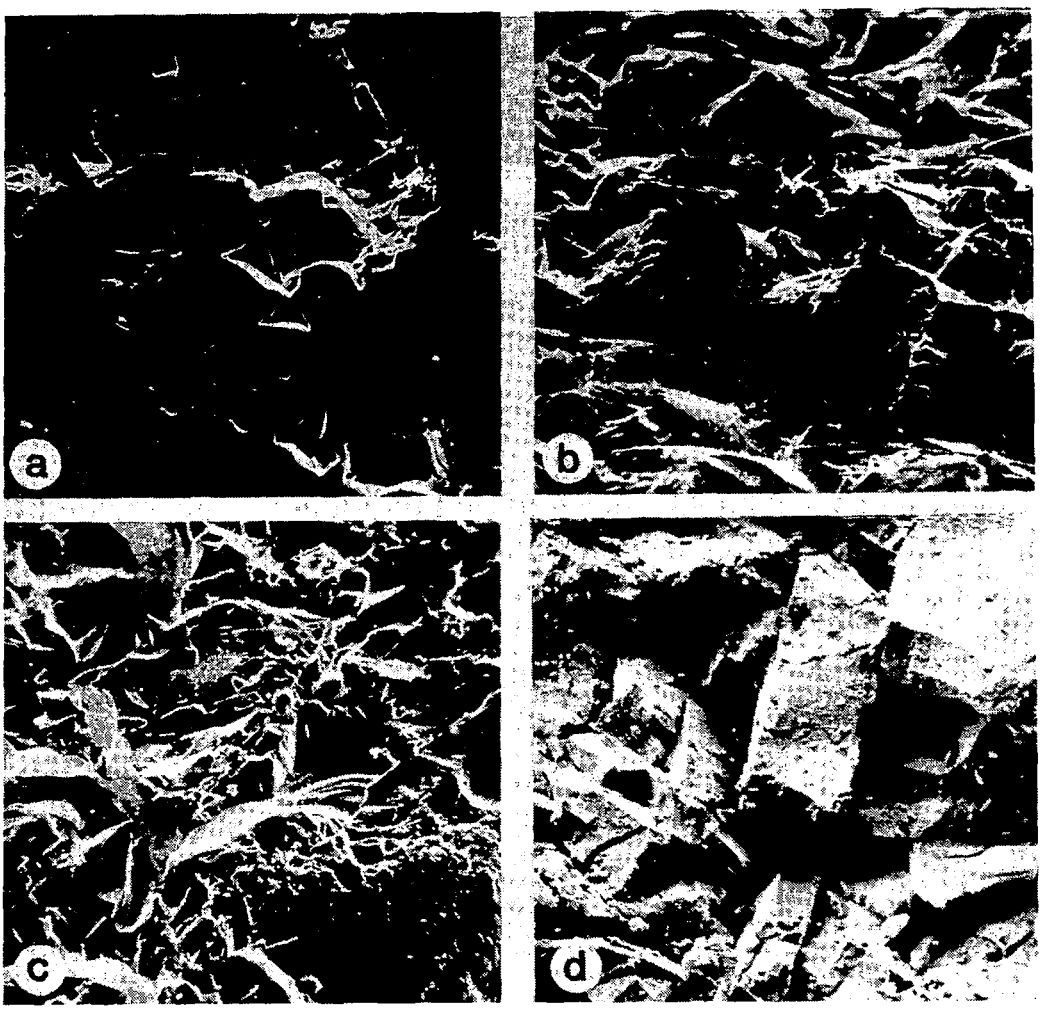

Figure 27. Stages in erosion of quartz plate, impacted by quartz particles 710-840 μm in diameter at speeds of 20 to 25 m/s, a) embryonic stage, showing triangular, crescentic, and polygonal depressions, b) youthful stage, showing surface represented by cone tops, c) advanced stage, showing curved escarpments, conchoidal fractures, irregular and cleavage-controlled fractures, and d) mature stage, showing blocky, cleavage-controlled structure. Frame widths are: a) 420 μm, b) 420 μm, c) 455 μm, and d) 150 μm.

giving the relationship

$$S_a \propto D_p^3 \qquad (35)$$

S_a Versus Particle Velocity

Figure 31 shows the effect of impact velocity on S_a for a wide range of rocks and materials; particle velocities ranged from 5 to 40 m/s. Particles were 125 to 180 μm quartz grains, impacting normal to the target in a CO_2 atmosphere at 5 mb pressure. Although the effect of particle velocity (v_p) is poorly defined for volcanic tuff (both welded and nonwelded) and rhyolite, the graphs for most materials show a slope of 2 on a log-log plot, giving the relationship

$$S_a \propto v_p^2 \qquad (36)$$

Combining relationships 23 and 24 gives

$$S_a \propto D_p^3 v_p^2 \quad (37)$$

which shows that mass lost per impact is directly proportional to the kinetic energy (KE) of the impacting particle.

$$KE = \tfrac{1}{2} m_p v_p^2, \; m_p \propto D_p^3$$

The very slight concave-upwards curvature of the size-effect plots and many of the velocity-effect plots is an indication that some factor other than kinetic energy may be involved. This may be the size of the contact area which increases with both velocity and particle size and increases in the number of pre-existing cracks encountered by the stress field. The behavior of brick apparently is due to the development of a sintered crust at low and medium velocities which chipped off in large pieces at high velocities.

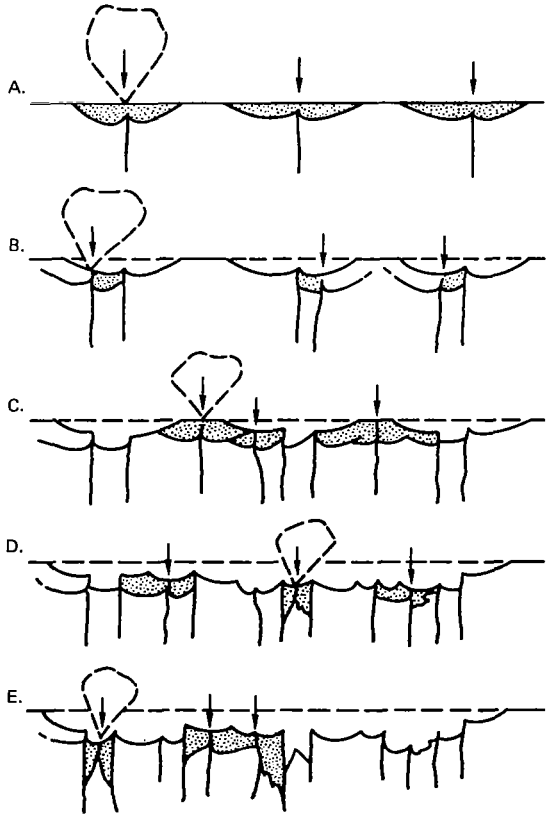

Figure 28. Possible fracturing and chipping sequence of a surface impacted with angular particles.

S_a Versus Particle Impact Angle

Figure 32 shows the effect of particle impact angle on S_a for the test materials; Figure 33 shows relative erosion as a function of impact angle of ideally ductile and brittle materials (after Oh et al., 1972) for comparison. Most of the rocks and materials tested appear to mimic a combination of typical brittle and ductile behavior, except obsidian which behaves as a brittle material.

The high susceptibility at low impact angles for some materials is interpreted as chipping and gouging of microblocks and the efficiency with which they are removed would increase as the angle declines. Fractures propagate to shallower depths as the vertical component of force diminishes. However, the high susceptibility at high angles suggests an apparent high ratio between indenter and target hardness which could lead to crushing and powdering of the surface at high impact angles. This may provide some degree of protection for the surface at normal (90°) impact and could account for the reduction in susceptibility. The downturn could also be due to impacting particles rebounding from the target and interfering with incoming particles, but this possibility has not been assessed fully.

S_a Versus Atmospheric Density

Tests to determine the effect of atmospheric pressure on abrasion (Fig. 34) were inconclusive. Generally at 1 bar there was slightly more erosion for the three materials tested than at martian pressure (5 mb). However, this may be related in some way to air turbulence in the confined abrasion chamber.

S_a Versus Particle Composition

Figure 35 shows S_a for basalt targets as a function of impact velocity for quartz, basalt, and basaltic ash particles 125 to 175 μm in diameter, impacting at 90°. Although

the data for basalt and ash particles are limited, there appears to be little difference in abrasion by quartz and basalt, whereas ash particles appear to be less effective as agents of abrasion.

Experiments were also conducted using aggregates as the agents of abrasion. A different apparatus than MRED was used, so the results are not entirely compatible for comparisons; however, the critical result

Figure 29. View of the apparatus used to conduct experiments to determine susceptibilities to erosion (S_a). Samples to be abraded are placed in holders (a) positioned within cylindrical chamber (b); cover for chamber (c) swings into position such that abrading particles (quartz sand, etc.) in hopper (d) are fed into rotating arm (e) where they are slung against the samples; speed of arm controls the impact velocity; sample holders (a) can be adjusted to control impact angle; 12 samples can be abraded per experiment; one sample station (f) is modified as an open port to collect the same amount of material as strikes each sample to enable an accurate determination of particle flux. Control panel is shown in foreground; chamber can be evacuated to low atmospheric densities and carbon dioxide can be introduced for martian simulations (from Greeley et al., 1982).

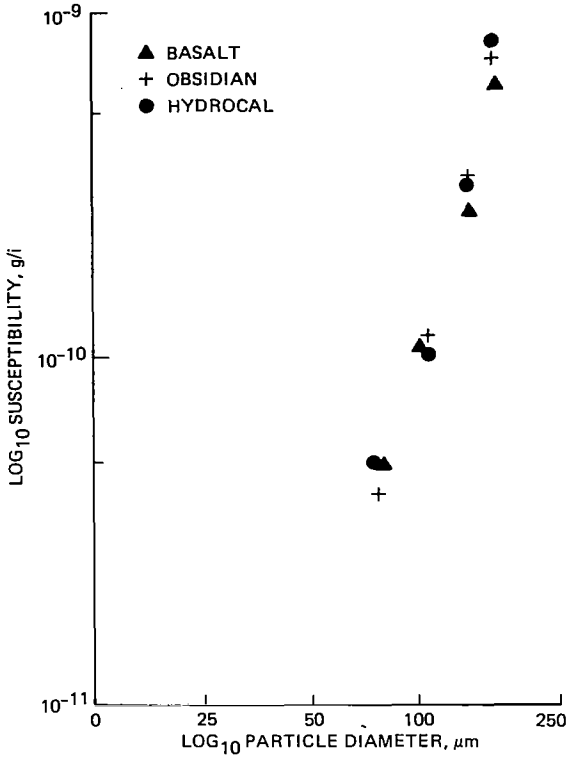

Figure 30. Susceptibilities to abrasion of basalt, obsidian, and hydrocal as a function of particle diameter; susceptibility (S_a) is expressed as the ratio of target mass eroded (g) to the number of impacting particles (i) (from Greeley et al., 1982).

was that for impact velocities below about 20 m/s, the aggregates were plastered against the target, causing a net gain in mass of the target and forming a protective coating. At higher impact velocities, the coating sloughed off, but there was no measurable loss in target mass.

4.4 SUMMARY

Susceptibility to abrasion is highly dependent on the texture of the rock, composition, velocity, and size of the impacting particles, and the angle of impact. On a per impact basis, glassy materials will erode very quickly for surfaces perpendicular to the wind; crystalline materials such as granite and basalt erode more quickly when surfaces are

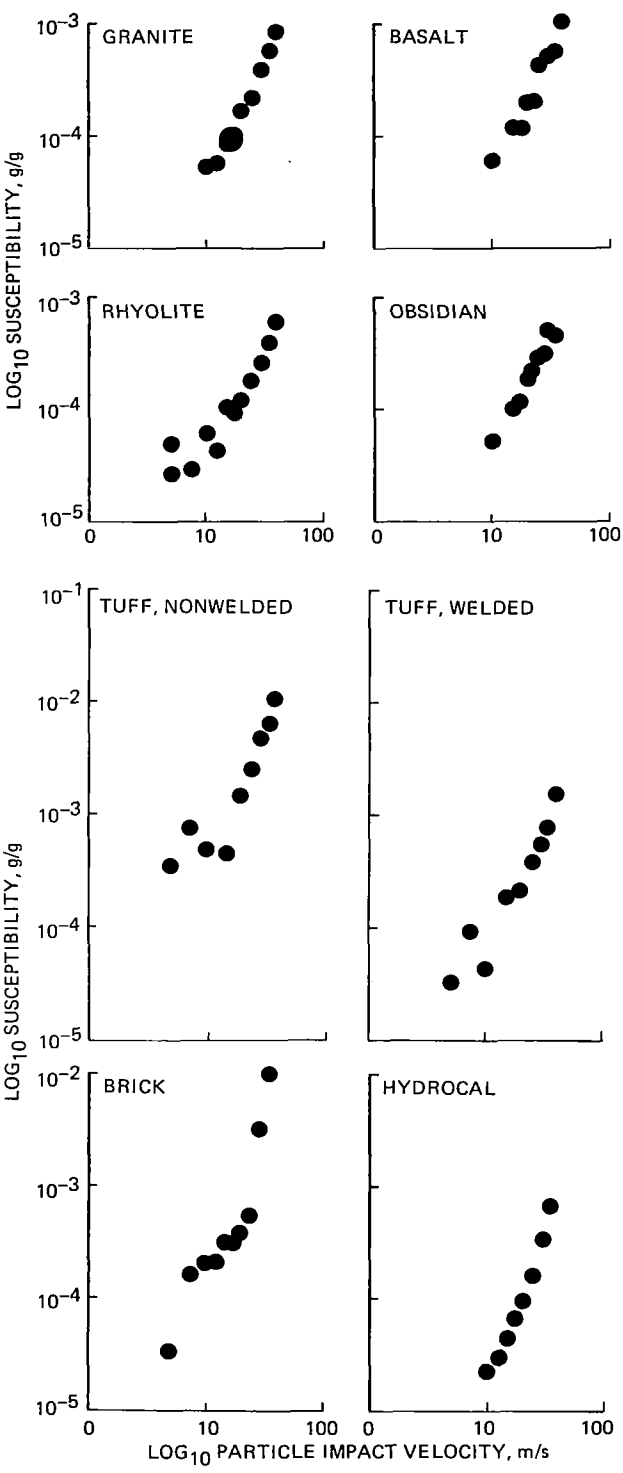

Figure 31. Susceptibilities to abrasion of test materials as functions of particle impact velocities (from Greeley et al., 1982).

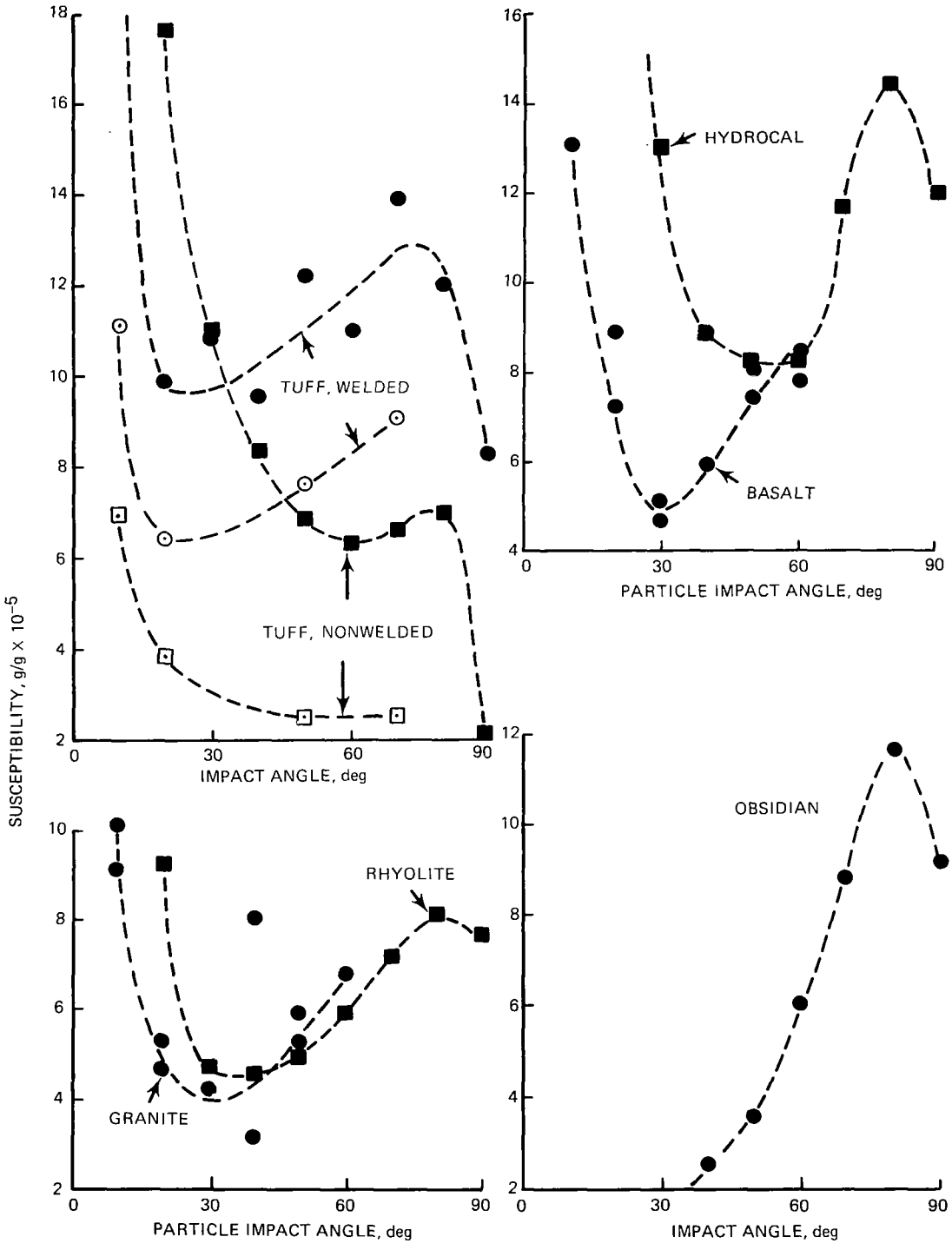

Figure 32. Susceptibilities to abrasion of test materials as functions of particle impact angle (from Greeley et al., 1982).

sub-parallel to the wind. Quartz and basalt grains appear to be of equal efficiency as agents of abrasion; basaltic ash is less efficient. Sand-size aggregates of fine grains do not abrade targets at low velocities, but form a veneer on the surface which shields the target from abrasion.

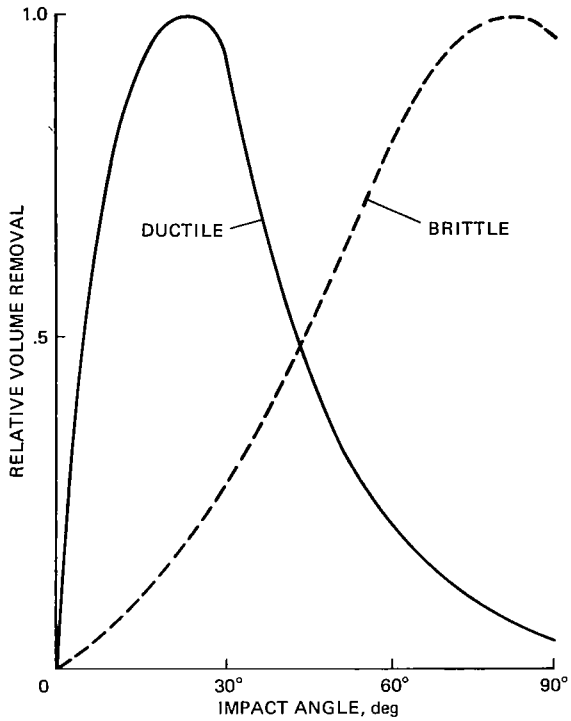

Figure 33. Relative erosion as a function of impact angle for typical brittle materials compared with ductile materials (after Oh et al., 1972). The downturn at 90° impact angle for brittle materials is due to two factors. The first is that at 90° impact, virtually all of the impactor KE goes into fracturing the surface and there is no lateral impetus to dislodge chips. The second is that, in abrasion machines and in nature, particles hitting a surface at 90° rebound straight back and interfere with incoming particles, protecting the surface from the full impact of subsequent impactors.

Figure 35. Susceptibility to abrasion of basalt as a function of impact velocity by 125 to 175 μm particles of quartz, basalt and basaltic ash (from Greeley et al., 1982).

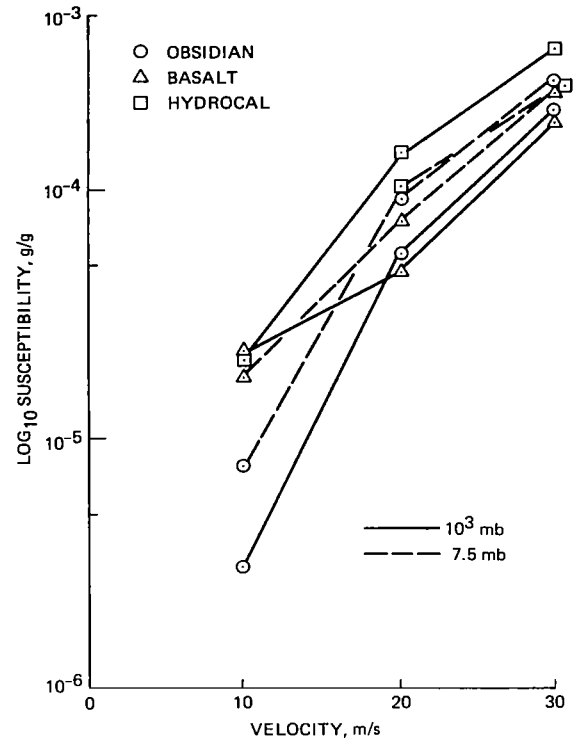

Figure 34. Susceptibility to abrasion for three materials as a function of impacting particles velocity in a 10^3 mb (Earth) pressure environment and 7.5 mb (Mars) pressure environment; although the data are limited, there is no apparent difference due to atmospheric density. S_a expressed as ratio of target mass loss to particle mass impacting the target.

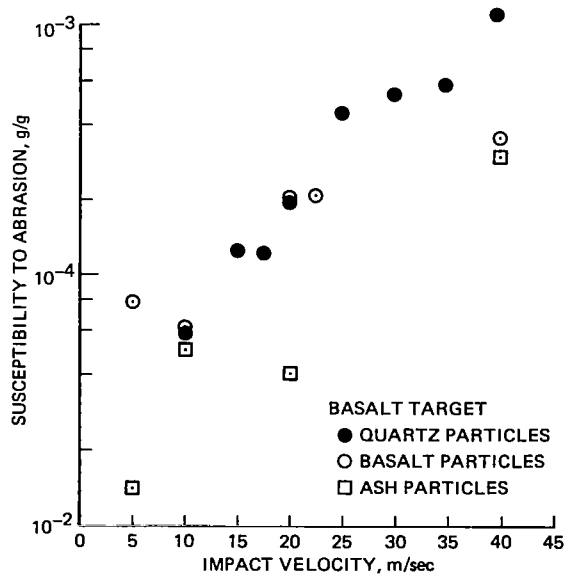

5. WIND FREQUENCY DATA

The third parameter required for estimating rates of aeolian abrasion involves various wind data, including wind directions, strengths, and durations. Ideally, wind data should also include velocity profiles so that surface shear stresses could be derived and utilized for particle threshold and particle flux analyses. In addition, wind data should be available for a sufficiently long period of time to characterize the local aeolian regime. Unfortunately, even minimal wind data are seldom available for sites of geologic interest and various techniques must be utilized to extrapolate from other areas.

5.1 TERRESTRIAL ENVIRONMENT

Wind data are usually obtained from meteorological stations, such as those associated with airports. Commonly, wind velocities with direction are determined for a single height – by convention 10 m above the ground – and reduced in the form of wind rose diagrams which show the frequency, velocities, and directions of winds for a given interval of time. Profiles of the wind velocity as functions of height are seldom obtained, yet this is the critical value for determining u_*.

In principle, it may be possible to extrapolate wind data from nearby recording stations to sites of interest. In practice such an extrapolation is difficult to achieve. One site where this was attempted is the Garnet Hill area in southern California, a classic ventifact locality (Blake, 1855). It is a site of frequent strong winds and active windblown sand. Sharp (1964, 1980) established long-term experiments to monitor the erosion of various rocks and man-made materials and to determine mass transport of windblown grains as a function of height above the ground. Particles were collected for intervals as long as four months, which integrated periods of wind activity with periods of quiescence. Unfortunately, on-site wind data were not obtained during the experiment, although Sharp recognized the desirability of such data.

The nearest meteorological station to Sharp's experimental site was the Palm Springs airport, about 9 km southeast of the site. The station has recorded winds for many years, including the interval covering Sharp's experiment. As part of a general study of ventifacts and other aeolian features at Garnet Hill, Hunter (1979) obtained wind data at Whitewater Wash in the fall and winter of 1977, near Sharp's site. Hunter's results confirmed Sharp's earlier speculations that the Palm Springs airport may not be in a favorable location for providing wind data appropriate for the experimental plot and demonstrates the difficulties in extrapolating wind data from one area to another.

5.2 MARTIAN ENVIRONMENT

During the past decade intensive observations of Mars have been made from Earth and from spacecraft which provide a variety of data that can be used to assess wind frequencies. Viking landers were equipped with meteorological instruments to provide data on the wind velocity, wind direction, and atmospheric temperature and pressure (Hess et al., 1976, 1977; Ryan et al., 1978) and provide direct information for two sites on Mars. Although Viking Lander 2 ceased operation in the late 1970s, Viking Lander 1, designated the Mutch Memorial Station, continued to monitor the winds and to obtain images until late 1982. The prominent winds compare favorably with aeolian features observed at the landing site (Binder et al., 1977) and from orbit (Greeley et al., 1978).

Observations from orbit provide additional clues to the frequency of threshold-strength winds. Relevant data include measurements of global and local dust storms and of albedo changes on the surface. Global dust storms apparently begin as local dust storms which originate at low or mid latitudes in the southern hemisphere during the summer. During the first martian year of the Viking mission, two global dust storms were observed, whereas only one such storm took place during the second martian year. Thus, threshold wind speeds are exceeded in the source regions of global dust storms with a frequency of about 3×10^{-2}, averaged over a martian year.

Strictly speaking, the term *global dust storm* refers only to suspended dust in the atmosphere. However, because supersonic winds would be required to place micron-sized dust directly into suspension (Pollack et al., 1976), undoubtedly saltation of ~100 μm sand grains also occurs whenever dust is raised into the atmosphere with the saltating grains aiding the infection of fine material into suspension through impact. Because much lower wind speeds are required for saltation to occur, the above estimate of the frequency of raising dust from the surface can also be considered to apply to the frequency of saltation.

Although our understanding of the mechanism by which global dust storms occur is still at a relatively rudimentary stage and strong differences of opinion exist, it seems likely that much of the martian surface serves as a source region for dust (Pollack et al., 1979; Leovy and Zurek, 1979). This viewpoint is also supported by the lack of a build-up of a superficial covering of fine dust from the decay of the global storms over much of the surface (Thomas and Veverka, 1979). However, the absence of appreciable albedo changes at the two lander sites during the global dust storms of the first martian year of the Viking mission (Guiness et al., 1979) indicates that dust was not raised over all the surface during the genesis of those storms. More generally, sand movement probably occurred to a greater degree in the southern hemisphere than the northern hemisphere (the two Viking landers are in the northern hemisphere), although precession will probably cause this enhanced sand motion to switch from the southern to the northern hemisphere and back with a cycle of $\sim 10^5$ years.

In addition to grain movement that occurs during global dust storms, movement occurs on local scales, as revealed by numerous local dust storms (Fig. 36) and by albedo changes of the surface. During the first martian year of the Viking mission, about 20 local dust storms were observed (Peterfreund and Kieffer, 1979). Allowing for incompleteness in coverage, perhaps 100 local dust storms actually took place during this time. A typical local dust storm covers an area between about 0.01 and 0.1% of the total martian surface and lasts for a few days.

Dark wind streaks tend to form behind topographic obstacles such as hills and crater rims (Thomas and Veverka, 1979). They are considered to form by wind erosion (Greeley et al., 1974) and thus serve to mark localities where saltation may occur more frequently than elsewhere. These streaks tend to be concentrated between 25° and 40° south latitude, although they may be found at all latitudes. Thus, saltation occurs more frequently in the lee of craters and ridges and in the upwind portion of crater interiors.

Most places on Mars are therefore subject to saltation at some time during each martian year, with the southern hemisphere experiencing greater activity. The considerations outlined here lead us to suggest that saltation takes place with a frequency ranging between about 1×10^{-2} and 1×10^{-1}, depending on the region.

Figure 36. Three local martian dust storms in Arcadia Planitia. Photos were taken with a violet filter during Revs 171-172, February 10, 1977. The largest is about 180 km in its longest dimension. Shadows along the northernmost cloud indicate a height of 5-10 km. (from Briggs et al., 1979).

5.3 SUMMARY

Very little direct information on wind frequencies is available for sites of geological interest on either Earth or Mars. Data which are available seldom cover a sufficiently long period of time to be meaningful in the geological context. For the most part, wind data on Earth must be extrapolated from meteorological stations to sites of interest. Because of the distances and/or varying terrain, such extrapolations allow, at best, only crude estimates of wind frequencies.

On Mars, wind frequency data can be obtained directly for two sites from measurements on the surface from the Viking landers, or indirectly through observations from orbit. However, poor knowledge of the surface roughness on Mars hampers translation of wind frequency data into values of threshold and particle flux.

6. RESULTS AND DISCUSSION

The previous three sections described the parameters involved in calculating rates of aeolian abrasion and present values for each parameter derived from experiments, field studies, and analytical models. These values are now used to estimate rates of abrasion on Earth and Mars.

6.1 AEOLIAN ABRASION ON EARTH

Although naturally occurring wind-abraded materials, such as ventifacts, have long been recognized and described (Blake, 1855; King, 1936; Sharp, 1949; and others), there have been relatively few attempts to determine rates of abrasion. Rates of abrasion can be derived from data provided from 5 studies, summarized in Table 3. However, lack of wind frequency data and information on particle flux prevent a rigorous quantitative assessment. The first study considered is that of Sharp (1949), in which ventifacts in the Big Horn Mountains, Wyoming are described. Rocks of several types were abraded (granite, gneiss, and quartzitic sandstone) and Sharp recognizes at least four separate periods of wind-cutting. The inferred rate is $\sim 10^{-3}$ cm/yr based on the estimated minimum abrasion averaged over the entire time since the initiation of wind-cutting the area.

Hickox (1959) studied ventifacts in the Annapolis Valley of Nova Scotia. The ventifacts are composed of vein quartz, quartzite, and indurated sandstone, and Hickox considered the ventifact faces to have formed in less than 10 years of exposure. The age is based on rocks that were quarried from a pit of known age.

McCauley et al. (1979) discovered sand-abraded hearth stones in Egypt considered to be of Upper Paleolithic age (200,000 years). The stones are abraded to a depth of 2 to 4 cm, yielding a rate of abrasion of 1 to 2 x 10^{-5} cm/yr.

From examination of a wind-abraded dacite boulder on one of the volcanic domes at Mono craters, California, and the estimated age of the domes, Williams (1981) obtained a rate of abrasion of $\sim 10^{-3}$ cm/yr.

TABLE 3. Rates of aeolian abrasion on Earth derived from ventifacts

LOCALITY	RATE	MATERIAL	REFERENCE
Big Horn Mountains, Wyoming	$\sim 10^{-3}$ cm/yr	gneiss	Sharp (1949)
Annapolis Valley, Nova Scotia	$\sim 10^{-1}$ cm/yr	quartzite, sandstone	Hickox (1959)
Western Egypt	1 to 2 x 10^{-5} cm/yr		McCauley et al. (1979)
Mono Craters, California	$\sim 10^{-3}$ cm/yr	dacite	Williams (1981)
Whitewater Wash, California	$\sim 6 \times 10^{-1}$ cm/yr $\sim 5 \times 10^{-1}$ cm/yr	brick hydrocal	Sharp (1964)

Sharp (1964) measured abrasion rates of relatively soft materials at Garnet Hill, California over an eleven year period. He found an abrasion rate of $\sim 6 \times 10^{-1}$ cm/yr for common red brick and $\sim 5 \times 10^{-1}$ cm/yr for hydrocal, a gypsum cement. Further study at the site (Sharp, 1980) showed a substantial increase in abrasion rate, due to the increased sand supply upwind of the abrasion test site caused by flooding of the Whitewater River.

The five cases described above have a range of rates from 10^{-5} to 6×10^{-1} cm/yr, and represent widely varying environments from cold and wet to hot and dry. These rates are comparable to those inferred by McCauley et al. (1981) and provide a basis for comparing rates and ages of surfaces described.

6.2 RATE OF WIND ABRASION ON MARS

Rates of wind abrasion at the VL-1 site on Mars can be estimated from saltation fluxes and wind frequencies (Table 4) and susceptibilities to abrasion for potential martian surface materials (Table 5). Basalt and hydrocal were considered as targets. Basalt is the most likely material present on the martian surface. Hydrocal was used as an analog to indurated clay which might also be on Mars. Several impactors were considered: quartz, basalt, basaltic ash, and aggregates composed of finer grains. All particles were ~ 100 μm in diameter, the size most easily moved on Mars (Fig. 3). For the calculation, abrasion of rocks was considered for a height of 10-12 cm above the surface, corresponding to the size of many rocks at the VL-1 site. Impacts were considered to occur normal to vertically oriented rock surfaces due to the flat trajectories of saltating particles on Mars.

In order to use the appropriate values for susceptibility to abrasion, particle velocities for measured winds at the VL-1 site must be determined. The winds measured at the VL-1 site are about 40% of the geostrophic wind speeds (Leovy and Zurek, 1979). The 25-30 m/s observed wind speeds thus imply a u_∞ = 62-75 m/s. This range is consistent with the upper dust cloud speed of 50 m/s observed over VL-1 when the near-surface winds of 25-30 m/s were recorded (James and Evans, 1981). For a height of 10-12 cm above the surface and a u_∞ = 70 m/s, we would expect the typical saltating particle to be moving at $\sim$30% of u_∞, or $\sim$20 m/s (Fig. 12).

The most difficult parameter to assess is the flux of saltating particles. The movement of particles at VL-1 would not be greatly inhibited by the presence of rocks. Even though rocks are common at VL-1, Moore et al. (1977) found that fine-grained material covers most of the surface and the rocks occupy less than 25% of the total area. On Earth, a comparable rock concentration would affect aeolian activity. Depending on the size and spacing of the rocks, particle movement could be enhanced in areas of high turbulence and retarded in wind 'shadows.' Because of the low martian atmospheric density, however, only surfaces with a roughness, z_o, greater than 1 cm would greatly affect particle motion. The value of z_o at VL-1 is only 0.1-1.0 cm (Sutton et al., 1978); hence, from the standpoint of particle movement, the VL-1 site should be the same as the 'sand only' case of Pollack et al. (1976). Therefore, the saltation flux equation of White (1979) can be used to calculate Q for VL-1 (Table 4). Since wind speeds measured at VL-1 rarely exceed threshold and then only slightly, a value of u_* 20% larger than u_{*t} was used for the calculation. Between 10-12 cm above the surface, q, the flux per unit area, is about 5% of Q, the flux per unit lane width (Fig. 18).

The remaining parameter required to calculate an aeolian abrasion rate is f, the frequency of saltation-strength winds. Although we have only limited meteorological

TABLE 4. Factors involved in estimating rates of aeolian abrasion at VL-1

FACTOR	VALUE	NOTES
Wind velocity u measured at VL-1	25-30 m/s	threshold strength (and strongest) winds measured at height of VL-1 anemometer (Hess et al., 1977; J.A. Ryan, personal communication, 1981)
Threshold velocity u_{*t}	1.25 m/s	for D_p = 100 μm, atmospheric surface pressure of 10 mb, 215 K (Greeley et al., 1980)
Shear velocity u_*	1.5 m/s	20% above threshold
Freestream velocity u_∞	70 m/s	based on $u = (0.4)(u_\infty)$ given by Leovy and Zurek (1979)
Wind frequency f	10^{-4}	frequency of winds 25-30 m/s (J.A. Ryan, personal communication, 1981)
Flux Q	1.3×10^{-1} g/cm•sec	calculated from White (1979) for $u_* = 1.5$ and $u_{*t} = 1.25$
Flux q at 10-12 cm height	6.6×10^{-3} g/cm^2•sec	at 10-12 cm above surface, q = (0.05) Q, shown in Figure 18
Particle velocity at 10-12 cm height	20 m/s	average particle velocity at height of 10-12 cm, $v_p = 0.3\ u_\infty$ (from Fig. 12)
Particle size D_p	100 μm	particle size most easily moved by lowest strength wind (from Fig. 3)
Impact angle	90°	for simplicity in the calculation, only 90° impacts were considered

data from VL-1, an upper value is $\sim 10^{-4}$ (J.A. Ryan, personal communication).

The rate of aeolian abrasion can be calculated for VL-1 from Equation (1) and Table 4. Typical rates at VL-1 for basalt targets are 3×10^{-10} gm/cm^2•sec, which is equivalent to 4×10^{-3} cm/yr. These rates are enormous and, if allowed to operate for any reasonable length of time, result in drastic modification of the rocks at VL-1, much more than is observed. Furthermore, the ejecta and rims of the small craters in the vicinity of VL-1 would also have been heavily eroded and/or buried unless they were very young. However, there is no model of surface rock production or recent impact cratering flux that would allow the VL-1 and orbiter observations and the high calculated abrasion rate all to be correct.

We consider several possible solutions to the discrepancy between observations of the surface and the calculated abrasion rate.

TABLE 5. Estimated rates of aeolian abrasion at VL-1

Target	Particle	S_a*	Abrasion Rate gm/cm^{2}s	Abrasion Rate cm/yr†
Basalt	quartz	2×10^{-4}	1×10^{-10}	2×10^{-3}
Basalt	basalt	2×10^{-4}	1×10^{-10}	2×10^{-3}
Basalt	ash	4×10^{-5}	3×10^{-11}	3×10^{-4}
Hydrocal	quartz	1×10^{-4}	6×10^{-11}	2×10^{-3}
Hydrocal	basalt	5×10^{-4}	3×10^{-10}	8×10^{-3}
Hydrocal	ash	3×10^{-4}	2×10^{-10}	5×10^{-3}

Rate = Susceptibility S_a x flux q x wind frequency f

* From MRED experiments

† Direct conversion from mass loss; does not take into account differences in abrasion resulting from varying impact angles

In order of increasing likelihood, these are: (1) climatic considerations, (2) surface history, and (3) factors dealing with the targets, particles, and particle mobility on Mars.

Climatic Effects

The estimated rates of aeolian abrasion given here assume present-day wind strengths and frequencies and other meteorological conditions. Yet the frequency of aeolian activity on Mars may have varied considerably over its history due to possible oscillatory and secular changes in atmospheric pressure. The oscillatory changes arise from astronomical variations in orbital and axial characteristics, whereas secular changes result from long term geochemical processes.

The atmospheric pressure at the surface, P_a, affects the frequency of aeolian activity due to the dependence of both the wind speed distributions function and the threshold wind speed, u_{*t}, on P_a. According to arguments advanced by Pollack (1979), the former is expected to change little for large changes in P_a about the current value. However, the measurements of Greeley et al. (1980) indicate that $u_{*t} \propto P_a^{-1/2}$, as shown in Figure 3. And as illustrated in Figure 3 and Equation 33, the frequency of aeolian activity depends very sensitively on u_{*t}, that is, at the current epoch it is only the relatively infrequent, highest wind speeds that set particles into motion. Thus if P_a is less than about 1/4 the current atmospheric pressure, no aeolian activity may occur; if it is an order of magnitude larger, aeolian activity may occur almost all the time.

Solar and planetary perturbations cause the eccentricity of Mars' orbit and the obliquity of its axis of rotation to undergo quasi-periodic oscillations on a time scale of 10^5 to 10^6 years and the orientation of its axis to precess with a period of 175,000 years, with the eccentricity and obliquity varying between extremes of 0 to 0.14 and 15 and 35°, respectively (Ward, 1974). It has been suggested that a large amount of CO_2, the principal atmospheric constituent, is currently contained in the subpolar regolith – about an

order of magnitude more CO_2 than is present in the atmosphere (Fanale and Cannon, 1979). At times of high obliquity, the annually averaged temperature at high latitudes increases and hence a larger amount of CO_2 is placed into the atmosphere and a smaller amount is taken up by the regolith. The opposite occurs at times of low obliquity, with the CO_2 being stored in permanent polar caps.

Measurements of CO_2 absorption onto fine-grained dust suggest that the atmospheric pressure could rise to values of about 20 mb (3 times the current value) at times of the highest obliquity and could decrease to values of less than 1 mb at times of the lowest obliquity, due to the formation of permanent CO_2 polar caps (Fanale and Cannon, 1979; Toon et al., 1980). Under these circumstances, no aeolian activity would be expected in the latter situation and a substantially elevated rate of aeolian activity – perhaps as much as an order of magnitude – would be expected in the former situation. However, it should be remembered that an enhanced level of aeolian activity may result mostly from the lowering of the threshold wind speed and thus involves chiefly lower wind speeds, for which erosion occurs at a diminished rate. Nevertheless, global dust storms will be more frequent and may involve wind speeds comparable to today's values due to dust-wind feedback relationships.

The precession of the axis of rotation causes a change in the relationship between seasons in a given hemisphere and the position of Mars in its orbit. At present, summer solstice in the southern hemisphere occurs at a time when Mars is close to its perihelion position. This relationship may be responsible for the apparently greater aeolian activity in the southern hemisphere than in the northern for the present epoch. If so, the northern hemisphere may have had greater aeolian activity half a precession cycle earlier (~100,000 years) and more generally this difference will vary in an oscillatory fashion.

Over the lifetime of Mars, a few bars of CO_2 – that is, about 300 times the amount now in the atmosphere – may have been outgassed from the planet's interior (Pollack and Black, 1979). Conceivably, much of the outgassed CO_2 remained in the atmosphere during the early history of Mars. However, due to the possible formation of carbonate rocks and the development of the regolith, the atmospheric pressure may have more or less monotonically declined with time over the last few billion years (Pollack and Yung, 1980). In this case, the level of aeolian activity may have been substantially higher in its past than at the present time. We can place an upper boundary on the amount of enhancement by supposing the global dust storms occurred all the time, but allowing enough time between successive storms for a given one to decay enough to permit the next to occur.

From these considerations of the climatic history of Mars, aeolian activity and abrasion could have been as much as an order of magnitude larger in the past than they are today. Thus, not only do climatic considerations fail to account for the discrepancy between the preservation of the surface and the present aeolian abrasion if holocrystalline materials were involved, these considerations drive the result in the opposite direction.

Surface History

The assumption is made that the surface of Chryse Planitia observed from orbit is very old because of the presence of abundant impact craters that were formed millions to hundreds of millions of years ago. These craters and the surface on which they occur could be preserved if they had been protected from the aeolian regime by a mantling deposit and then recently exhumed, as proposed by Sagan et al. (1977) and Binder et al. (1977). Much of Mars appears to be mantled by deposits of unknown origin, as first proposed by Soderblom et al. (1973) based on Mariner 9

results. The characteristics of the mantling deposits suggest to most investigations (reviewed by Carr, 1981) that they are of aeolian origin and probably resulted from deposition of fine-grained materials from dust storms.

Viking Orbiter images show many parts of Mars that have been mantled and exhumed, as shown in Figure 37. The impact crater in this figure has been partly exhumed, note that rather fine detail has been preserved in the ejecta field. Were it not for the fact that part of the crater remains buried, it is unlikely that the crater and surrounding surface would have given any evidence of having been mantled.

Parts of Chryse Planitia, site of the Viking Lander 1, also show evidence of having been mantled and partly exhumed, as noted by Greeley et al. (1977b). Furthermore, the deposits of fine-grained debris observed from the Viking 1 lander (Fig. 5) have been described as drifts of aeolian deposits that have been eroded (Mutch et al., 1976). These deposits could be the last remnant of a much more extensive mantle (Sharp and Malin, 1983).

On Earth, exhumed surfaces formerly blanketed with aeolian deposits can reveal features of pristine form. Figure 38 shows a basaltic plain in Iceland that was buried by loess to a depth of several meters. The area is currently undergoing deflation and the basaltic flows are being exhumed. Fine structure on the scale of centimeters, such as pahoehoe ropes, has been preserved by the loess and despite the extensive aeolian activity required for deflation, remains in excellent condition.

Thus, mantling of the cratered basaltic plains of Chryse Planitia and subsequent exhumation millions or hundreds of millions of years later could explain both the high current calculated rate of abrasion and the preservation of the cratered surface. However, high resolution Viking Orbiter images show that many areas of Mars preserve small, ancient impact craters, and it seems unlikely that all such areas could be explained by exhumation because there are no known 'sinks' that could accomodate the volume of deflated sediments. Further, the large calculated abrasion rates at VL-1 would imply that stripping occurred at that site in the very recent ($\sim 10^6$ years) past, perhaps unreasonably recent.

Material Properties

Rates of aeolian abrasion are partly determined by the material properties of both the target and the windblown particles. Despite all evidence to the contrary, perhaps the bedrock material on Mars is not basalt, but some other extremely resistant rock. However, we determined the susceptibilities to abrasion for a wide variety of common rocks (Table 2), and even the most resistant yield a very high rate of abrasion for Mars. Thus, the bedrock would have to be something completely foreign to terrestrial experience; from petrological considerations this seems highly unlikely.

Agents of Abrasion

The calculated aeolian abrasion rate is based on the assumption of an unlimited and unrestricted sand supply. If there is little sand in the system, abrasion will occur only at a greatly reduced rate. There is a considerable amount of sand sized material on Mars, as shown by the IRTM (Christensen, 1983) and as inferred from the presence of dunes and dune fields (Tsoar et al., 1979). However, the sand supply at the Viking sites could be limited. It is also possible that the free movement of sand is inhibited by the presence of cohesion in the uppermost layer, as perhaps inferred by the structure of the slump in a drift at VL-1 (Binder et al., 1977), or by the

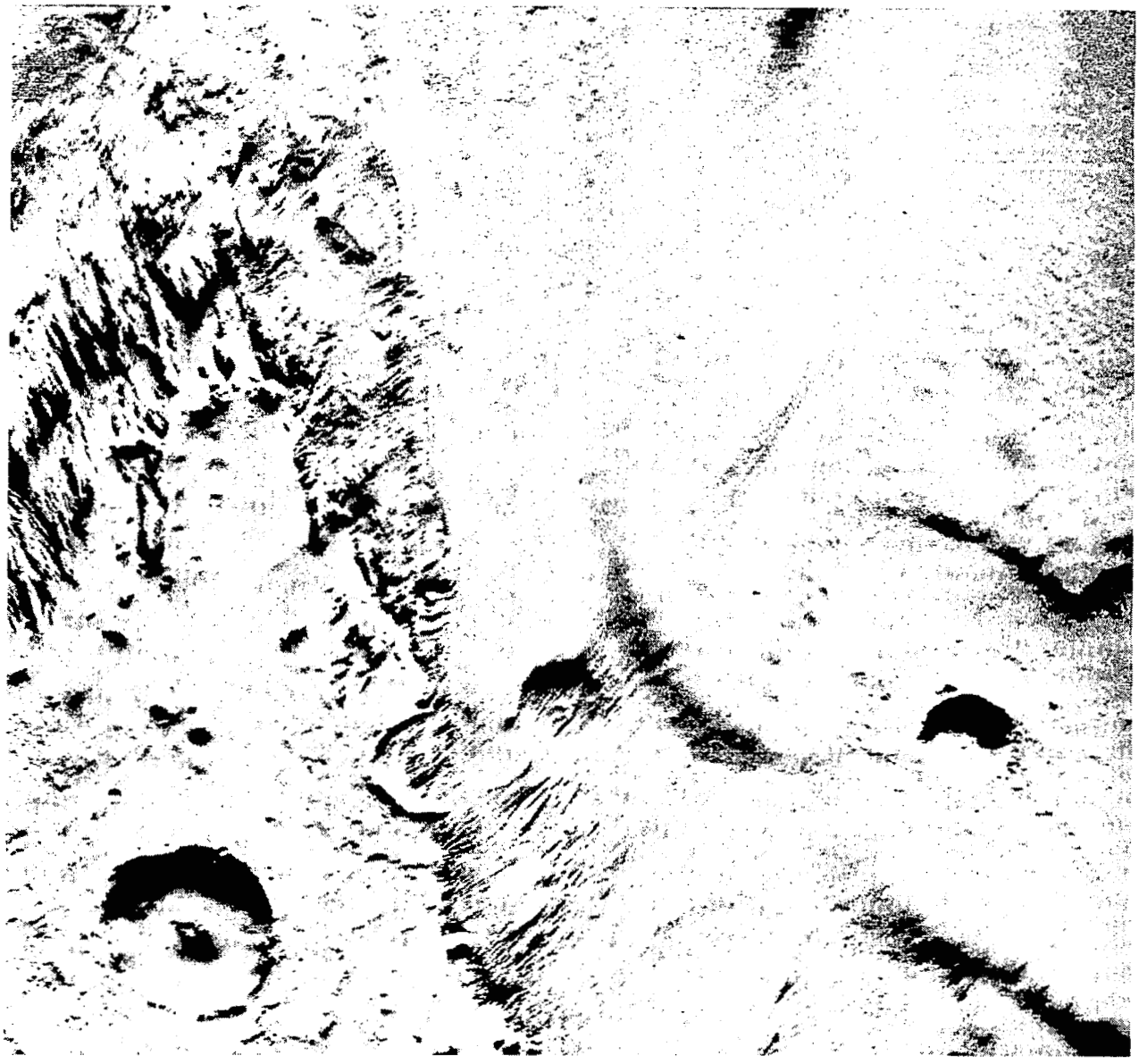

Figure 37. Martian landscape showing aeolian mantle being stripped away, exhuming craters (Viking frame 438S01). The width of the frame is approximately 75 km.

protection of the sand from the wind by a dust fallout deposit. The dust would be difficult to move because of its small grain size and the corresponding large u_{*t} needed to initiate movement (Christensen, 1982).

Another important factor is the composition of the abrasion agent. Figure 35 shows S_a values based on abrasion by quartz sand, basalt grains, and basaltic ash – all of about 150 μm in diameter and all striking the same target type at the same velocity. Quartz and basalt grains are roughly comparable in their ability to abrade. Although basaltic ash appears to be less effective than quartz or basalt by a factor of about 2, rates of abrasion based on basaltic ash are still much higher

Figure 38. Basalt lava flows in Iceland, northwest of Askja volcano, were buried by windblown silt to a depth exceeding 2 m and are currently being exhumed by deflation of the silt; primary flow features as small as a centimeter remain on the exhumed surfaces, evidenced by the pahoehoe ropes seen in the foreground. Mushroom-shaped features to the left of figure on horizon is remnant of aeolian silt not yet eroded.

than would be reasonable, based on the age of the cratered surface. However, as discussed in Section 4, aggregates of fine material are very inefficient as agents of abrasion. At particle speeds lower than about 15 m/s, aggregates form a veneer on the target surface (Greeley et al., 1982). Abrasion does not occur until velocities greater than 15 m/s are achieved. Average particle speeds in this range on Mars require freestream wind speeds in excess of 75 m/s. The maximum inferred geostrophic winds measured at the Viking Lander site are only about 62-75 m/s. Although wind speeds higher than those measured at the landing sites are predicted for other areas on Mars based on the global circulation model of Pollack et al. (1981), the frequency of geostrophic winds exceeding 75 m/s is extremely low.

Conclusions

Calculations of present rates of aeolian abrasion yield unreasonably high values for the Viking landing sites when based on impacting grains composed of holocrystalline grains or basaltic ash. However, the surface displays an impact crater distribution that indicates its age to be several hundred million years old. The presence of the craters and blocks that are relatively unmodified on a surface of great

age, argue against a continuous high abrasion rate. Although there are many uncertainties and assumptions in the analysis, we consider the best explanation for this discrepancy to be a combination of factors dealing with the particles and the surface history, at least for the region surrounding the Viking Lander 1 site. A model has been proposed (Greeley, 1979; Greeley and Leach, 1978) which suggests that fine particles ($\sim$ few μm) derived from the frequent dust storms and the rapid attrition of larger grains would aggregate to form sand-size grains. Such aggregates are found to be very inefficient agents of abrasion at the low wind speeds typical for Mars. However, some sand of holocrystalline grains are undoubtedly present, as evidenced by the presence of dunes on Mars. Thus, over the long period since the craters were formed, we consider that there would have been more erosion than is apparent. Thus, given the photogeological evidence for mantling, we also consider the surface was covered with a blanket of sediments and effectively shielded from erosion.

ACKNOWLEDGMENTS

This work began in 1974 when it became apparent that knowledge of rates of wind erosion was essential to understanding the surface history of Mars. Because of the complexity of the problem, it was decided to use a team approach. Experiments to determine the susceptibility to abrasion for different materials began with fabrication of a device to simulate aeolian abrasion under terrestrial and martian conditions by R. Leach and the instrument shops at NASA-Ames Research Center. Several different machines were tested, each contributing solutions to different parts of the problem. During the early phase W. McKinnon, then a student at the California Institute of Technology, carried out tests partly to determine the procedure for using laboratory devices for abrasion studies. He was followed by S. Williams (then a NASA Planetary Geology summer intern) who initiated systematic abrasion studies of rocks. Concurrently, R. Leach conducted experiments on the erosion of the aeolian particles. In 1975 D. Krinsley began SEM studies of both the particles and abraded rocks to compare their surfaces with geological materials that had been abraded under natural conditions in order to verify the use of laboratory devices. The final machine used in most of the abrasion studies is based on a design used at the Argonne National Laboratory for material testing, and was the result of efforts by T. McKee and D. Hamilton, both of Arizona State University. S. Williams and G. Stewart completed the series of abrasion experiments as part of their graduate studies.

Parallel with the investigations of aeolian abrasion, wind tunnel experiments were conducted to determine various particle parameters under Earth and martian environments. Using a design by R. Leach, in 1977 J. Burt from the California Institute of Technology fabricated a particle collector and carried out a series of tests on particle flux. Subsequent analyses of the results led to redesign of the collectors; the final collectors were tested using a smoke wind tunnel at the University of California (Davis) to determine the most effective shape for collecting the particles with least disruption to air flow. Data were then systematically collected in the wind tunnel, first by M. Niemiller and M. Plummer, University of Santa Clara, then by K. Malone, a NASA Planetary Geology summer intern. Particle velocity measurements were made in wind tunnel tests using a device modified by R. Leach and the NASA-Ames instrument shops from a similar device used by the U.S. Forest Service to measure windblown snow particles. Experiments were conducted by R. Leach, K. Malone, and R. Leonard. Particle trajectories and velocities were determined by B. White and J. Schulz from high speed motion pictures obtained by the Photographic Technology Branch at NASA-Ames. Computational models of particle motion were developed by B. White. J. Marshall determined the manner in which geological materials abrade on the microscopic scale.

We thank Jack McCauley for his review of this manuscript and helpful discussion regarding wind erosion.

All phases of the work were supported by the Planetary Geology Program, National Aeronautics and Space Administration, Washington, D.C., through Ames Research Center.

REFERENCES

Adler, W.F., 1974. Erosion of fused silica by glass beads, *in Erosion, Wear, and Interface with Corrosion,* Am. Soc. Test. Mater., Spec. Tech. Publ.

Adler, W.F., 1976a. Analysis of particulate erosion, *Wear, 37,* 345-352.

Adler, W.F., 1976b. Analytical modeling of multiple particle impacts on brittle materials, *Wear, 37,* 353-364.

Andrews, J.P., 1931. Percussion figures, *Proc. Phys. Soc. London, 43,* 18-25.

Arvidson, R., E. Guinness, and S. Lee, 1979. Differential aeolian redistribution rates on Mars, *Nature, 278,* 533-535.

Bagnold, R.A., 1941. *The Physics of Blown Sand and Desert Dunes,* Methuen, London.

Binder, A.B., R.E. Arvidson, E.A. Guinness, K.L. Jones, E.C. Morris, T.A. Mutch, D.C. Pieri, and C. Sagan, 1977. The geology of the Viking Lander 1 site, *J. Geophys. Res., 82,* 4439-4451.

Blake, W.P., 1855. On the grooving and polishing of hard rocks and minerals by dry sand, *Am. J. Sci., 20,* 2nd series, 178-181.

Briggs, G.A., W.A. Baum, and J. Barnes, 1979. Viking Orbiter imaging observations of dust in the martian atmosphere, *J. Geophys. Res., 84,* 2795-2820.

Carr, M.H., 1981. *The Surface of Mars,* Yale University Press, New Haven, Conn.

Christensen, P.R., 1982. Martian dust mantling and surface composition: Interpretation of thermophysical properties, *J. Geophys. Res., 87,* no. B12, 9985-9998.

Christensen, P.R., 1983. Aeolian intercrater deposits on Mars: Physical properties and global distribution, submitted to *Icarus.*

Cutts, J.A., 1973. Wind erosion in the Martian polar regions, *J. Geophys. Res., 78,* 4211-4221.

Cutts, J.A., and R.S.U. Smith, 1973. Eolian deposits and dunes on Mars, *J. Geophys. Res., 78,* 4139-4154.

Fanale, F.P., and W.A. Cannon, 1979. Mars: CO_2 absorption and capillary condensation of clays – significance for volatile storage and atmospheric history, *J. Geophys. Res., 84,* 8404-8414.

Finnie, I., 1960, Erosion of surfaces by solid particles, *Wear, 3,* 87-103.

Goudie, A.S., R.U. Cooke, and J.C. Doornkamp, 1979. The formation of silt from quartz dune sand by salt-weathering processes in deserts, *J. Arid Environments, 2,* 105-112.

Greeley, R., 1979. Silt-clay aggregates on Mars, *J. Geophys. Res., 84,* 6248-6254.

Greeley, R., J.D. Iversen, J.B. Pollack, N. Udovich, and B. White, 1974. Wind tunnel simulations of light and dark streaks on Mars, *Science, 183,* 847-849.

Greeley, R., B.R. White, J.B. Pollack, J.D. Iversen, and R.N. Leach, 1977a. Dust storms of Mars: Considerations and simulations, *NASA Tech. Memo., TM 78423.*

Greeley, R., E. Theilig, J.E. Guest, M.H. Carr, H. Masursky, and J.A. Cutts, 1977b. Geology of Chryse Planitia, *J. Geophys. Res., 82,* 4093-4109.

Greeley, R., and R. Leach, 1978. A preliminary assessment of the affects of electrostatics on aeolian processes, *Rept. Plan. Geol. Prog.* 1977-1978, NASA TM-79729, 236-237.

Greeley, R., R. Papson, and J. Veverka, 1978. Crater streaks in the Chryse Planitia region of Mars: Early Viking results, *Icarus, 34,* 556-567.

Greeley, R., R.N. Leach, B.R. White, J.D. Iversen, and J.B. Pollack, 1980. Threshold windspeeds for sand on Mars: Wind tunnel simulations, *Geophys. Res. Lett., 7,* 121-124.

Greeley, R., B.R. White, J.B. Pollack, J.D. Iversen, and R.N. Leach, 1981. Dust storms of Mars: Considerations and simulations, *Geol. Soc. Am. Spec. Publ. 186,* 101-121.

Greeley, R., and P.D. Spudis, 1981. Volcanism on Mars, *Rev. Geophys. Space Phys., 19,* 13-41.

Greeley, R., R.N. Leach, S.H. Williams, B.R. White, J.B. Pollack, D.H. Krinsley, and J.R. Marshall, 1982. Rate of wind abrasion on Mars, *J. Geophys. Res., 87,* no. B12, 10,009-10,024.

Greeley, R., S.H. Williams, and J.R. Marshall, 1983. Velocities of windblown particles in saltation: Preliminary laboratory and field measurements, *Proc. 11th Int. Congress on Sedimentology* (in press).

Guinness, E.A., R.E. Arvidson, D.C. Gehret, and L.K. Bolef, 1979. Color changes at the Viking landing sites over a course of a Mars year, *J. Geophys. Res., 84,* no. B14, 8355-8364.

Henry, R.M., 1975. Saltation on Mars and expected lifetime of Viking 75 wind sensors, *NASA Tech. Note, D-8035,* 39 pp.

Hess, S.L., R.M. Henry, C.B. Leovy, J.L. Mitchell, J.A. Ryan, and J.E. Tillman, 1976. Early meteorological results from the Viking 2 lander, *Science, 184,* 1352.

Hess, S.L., R.M. Henry, C.B. Leovy, J.A. Ryan, and J.E. Tillman, 1977. Meteorological results from the surface of Mars: Viking 1 and 2, *J. Geophys. Res., 82,* 4559-4574.

Hickox, C.F., 1959. Formation of ventifacts in a moist, temperate climate, *Geol. Soc. Am. Bull., 70,* 1489-1490.

Huffman, G.G., and W.A. Price, 1949. Clay dune formation near Corpus Christi, Texas, *J. Sed. Pet., 19,* 118-127.

Hunter, W.A., 1979. Ventifacts on Garnet Hill, unpublished senior thesis, Dept. of Earth Sciences, Cal. State Polytechnic Univ., Pomona, 223 pp.

Iversen, J.D., J.B. Pollack, R. Greeley, and B.R. White, 1976. Saltation threshold on Mars: The effect of interparticle force, surface roughness, and low atmospheric density, *Icarus, 29,* 381-393.

James, P.B., and N. Evans, 1981. A local dust storm in the Chryse region of Mars: Viking orbiter observations, *Geophys. Res. Lett., 8,* 903-906.

Johnson, K.L., J.J. O'Connor, and A.C. Woodward, 1973. The effect of the indenter elasticity on the Hertzian fracture of brittle materials, *Proc. Royal Soc. London, A, 334,* 95-117.

Kawamura, R., 1951. Study on sand movement by wind, *Inst. of Science and Technology,* Tokyo, Report 5, 95-112.

King, I.C., 1936. Wind-faceted stones from Marlborough, New Zealand, *J. Geol., 44,* 201-213.

Knight, C.G., M.V. Swain, and M.N. Chaudhri, 1977. Impact of small steel spheres on glass surfaces, *J. Mat. Sci., 12,* 1573-1586.

Krinsley, D.H., J.H. Fink, and R. Greeley, 1980. Explosive volcanism: Possible source of aggregate formation on Mars, *EOS, Trans. Am. Geophys. Union* (abst.), *61,* no. 46, 1138.

Kuenen, Ph.H., 1960. Experimental abrasion 4: Eolian action, *Journal of Geology, 68,* 427-449.

Lawn, B., and R. Wilshaw, 1975. Review – indentation fracture: principles and applications, *J. Material Science, 10,* 1049-1081.

Leovy, C.B., and R.W. Zurek, 1979. Thermal tides and martian dust storms: Direct evidence for coupling, *J. Geophys. Res., 84,* 2956-2968.

Lobeck, A.K., 1939. *Geomorphology,* McGraw-Hill, New York, 731 pp.

Malin, M.D., 1974. Salt weathering on Mars, *J. Geophys. Res., 79,* 3888-3894.

Marshall, J.R., 1979. The simulation of sand grain surface textures using a pneumatic gun and quartz plates, Ph.D. thesis, Univ. College, London.

McCauley, J.F., 1973. Mariner 9 evidence for wind erosion in the equatorial and mid-latitude regions of Mars, *J. Geophys. Res., 78,* 4123-4137.

McCauley, J.F., C.S. Breed, F. El-Baz, M.I. Whitney, M.J. Grolier, and A.W. Ward, 1979. Pitted and fluted rocks in the Western Desert of Egypt: Viking comparisons, *J. Geophys. Res., 84,* 8222-8231.

McCauley, J.F., C.S. Breed, and M.C. Grolier, 1981. The interplay of fluvial, mass-wasting and eolian processes in the eastern Gilf Kebir region, *Annals of the Geological Survey of Egypt, 11,* 207-239.

McLaughlin, D., 1954. Volcanism and aeolian deposition on Mars, *Bull. Geol. Soc. Amer., 65,* 715-717.

Mills, A.A., 1977. Dust clouds and frictional generation of glow discharges on Mars, *Nature, 268,* 614.

Moore, H.J., R. Hutton, C. Scott, C. Spitzer, and R. Shorthill, 1977. Surface materials of the Viking landing sites, *J. Geophys. Res., 82,* 4497-4523.

Morsi, S.A., and A.J. Alexander, 1972. An investigation of particle trajectories in two-phase flow systems, *J. Fluid Mech.,* part 2, *55,* 193-208.

Mutch, T.A., R.A. Arvidson, A.B. Binder, F.O. Huck, E.C. Levinthal, S. Liebes, E.C. Morris, D. Nummendal, J.B. Pollack, and C. Sagan, 1976. Fine particles on Mars: Observations with the Viking 1 lander cameras, *Science, 194,* 87-91.

Neilson, J.H., and A. Gilchrist, 1968. Erosion by a stream of solid particles, *Wear, 11,* 111-122.

Oh, H.L., K.P.L. Oh, S. Vaidyanathan, and I. Finnie, 1972. On the shaping of brittle solids by erosion and ultrasonic cutting, Proceedings of the Symposium on the Science of Ceramic Machining and Surface Finishing, *U.S. Natl. Bur. Stand. Spec. Publ., 348,* 119-132.

Peterfreund, A.R., 1981. Visual and infrared observations of wind streaks on Mars, *Icarus, 45,* no. 2, 447-467.

Peterfreund, A.R., and H.H. Kieffer, 1979. Thermal infrared properties of the martian atmosphere 3, local dust clouds, *J. Geophys. Res., 84,* 2853-2864.

Pettijohn, F.J., P.E. Potter, and R. Siever, 1972. *Sand and sandstone,* Springer-Verlag, New York, 618 pp.

Pollack, J.B., 1979. Climatic change on the terrestrial planets, *Icarus, 37,* 479-553.

Pollack, J.B., R. Haberle, R. Greeley, and J. Iversen, 1976. Estimates of the wind speeds required for particle motion on Mars, *Icarus, 29,* 395-417.

Pollack, J.B., and D.C. Black, 1979. Implications of the gas compositional measurements of Pioneer Venus for the origin of planetary atmospheres, *Science, 205,* 56-69.

Pollack, J.B., D.S. Colburn, F.M. Flasar, R. Kahn, C.E. Carlson, and D. Pidek, 1979. Properties and effects of dust particles suspended in the Martian atmosphere, *J. Geophys. Res., 84,* 2929-2945.

Pollack, J.B., and Y.L. Yung, 1980. Origin and evolution of planetary atmospheres, *Ann. Rev. Earth Planet. Sci., 8,* 425-487.

Pollack, J.B., C.B. Leovy, P.W. Greiman, and Y. Mintz, 1981. A martian general circulation experiment with large topography, *J. Atmos. Sci., 38,* 3-29.

Ryan, J.A., R.M. Henry, S.L. Hess, C.B. Leovy, J.E. Tillman, and C. Walcek, 1978. Mars meteorology: Three seasons at the surface, *Geophys. Res. Lett., 5,* 715-718.

Sagan, C., 1973. Sandstorms and eolian erosion on Mars, *J. Geophys. Res., 78,* 4155-4161.

Sagan, C., J. Veverka, P. Fox, R. Dubisch, J. Lederberg, E. Levinthal, L. Quam, R. Tucker, J.B. Pollack, and B.A. Smith, 1972. Variable features on Mars: preliminary Mariner 9 television results, *Icarus, 17,* 346-372.

Sagan, C., D. Pieri, P. Fox, R. Arvidson, and E. Guinness, 1977. Particle motion on Mars inferred from the Viking lander cameras, *J. Geophys. Res., 82,* 4430-4438.

Schmidt, R.A., 1977. A system that measures blowing snow, *Res. Pap. RM-194,* U.S. Dept. of Agric., Washington, D.C., 80 pp.

Scott, D.H., and M.H. Carr, 1978. Geological map of Mars, U.S. Geol. Survey, Misc. Geol. Inv. Map I-1083.

Sharp, R.P., 1949. Pleistocene ventifacts east of the Big Horn Mountains, Wyoming, *J. Geol., 57,* 175-195.

Sharp, R.P., 1964. Wind-driven sand in Coachella Valley, California, *Geol. Soc. Am. Bull., 75,* 785-804.

Sharp, R.P., 1980. Wind-driven sand in Coachella Valley, California: Further data, *Geol. Soc. Am. Bull., 91,* 724-730.

Sharp, R.P. and M.C. Malin, 1983. Geology from the Viking Landers on Mars: a second look, *Bull. Geol. Soc. Amer.,* in press.

Sheldon, G.L., 1970. Similarities and differences in the erosion behavior of materials, *Trans. ASME, J. Basic Eng., 92,* 619-626.

Sheldon, G.L., and I. Finnie, 1966a. On the ductile behavior of nominally brittle materials during erosive cutting, *Trans. ASME, J. Eng. Ind.,* Nov., 387-392.

Sheldon, G.L., and I. Finnie, 1966b. The mechanism of material removal in the erosive cutting of brittle materials, *Trans. ASME, J. Eng. Ind.,* Nov., 393-400.

Sheldon, G.L., and A. Kanhere, 1972. An investigation of impingement erosion using single particles, *Wear, 21,* 195-200.

Singer, R.B., T.B. McCord, R.N. Clark, J.B. Adams, and R.L. Huguenin, 1979. Mars surface composition from reflectance spectroscopy: A summary, *J. Geophys. Res., 84,* 8415-8487.

Smalley, I.J., and D.H. Krinsley, 1979. Aeolian sedimentation on earth and Mars: Some comparisons, *Icarus, 40,* 276-288.

Smeltzer, C.E., M.E. Goulden, and W.A. Compton, 1970. Mechanism of metal removal by impacting dust particles, *Trans. ASME, J. Basic Eng.,* Sept., 639-654.

Soderblom, L.A., M.C. Malin, J.A. Cutts, and B.C. Murray, 1973. Mariner 9 observations of the surface of Mars in the north polar regions, *J. Geophys. Res., 78,* 4197-4210.

Sutton, J.L., C.B. Leovy, and J.E. Tillman, 1978. Diurnal variations of the martian surface layer meteorological parameters during the first 45 sols at two Viking lander sites, *J. Atmos. Sci., 35,* 2346-2355.

Suzuki, T., and K. Takahashi, 1981. An experimental study of wind abrasion, *J. Geol., 89,* 509-522.

Thomas, P., and J. Veverka, 1979. Seasonal and secular variations of wind streaks on Mars: an analysis of Mariner 9 and Viking data, *J. Geophys. Res., 84,* 8131-8146.

Tillett, J.P.A., 1956. Fracture of glass by spherical indentures, *Proc. Phys. Soc., B69,* 47-54.

Tilly, G.P., 1969. Erosion caused by airborne particles, *Wear, 14,* 63-79.

Tilly, G.P., and W. Sage, 1970. The interaction of particle and material behavior in erosion processes, *Wear, 16,* 447-465.

Toon, O.B., J.B. Pollack, W. Ward, J. Burns, and K. Bilski, 1980. The astronomical theory of climatic change on Mars, *Icarus, 44,* 552-607.

Toulman, P., III, A.K. Baird, B.C. Clark, K. Heil, H.J. Rose, R.P. Christian, P.H. Evans, and W.C. Kelliher, 1977. Geochemical and mineralogic interpretations of the Viking inorganic chemical results, *J. Geophys. Res., 82,* 4625-4634.

Tsoar, H., R. Greeley, and A.R. Peterfreund, 1979. Mars: the north polar sand sea and related wind patterns, *J. Geophys. Res., 84,* 8167-8180.

Tsuchiya, Y., 1969. Mechanics of the successive saltation of a sand particle on a granular bed in a turbulent stream, *Disas. Prev. Res. Inst. Kyoto Univ., Bull., 19,* part 1(152), 31-44.

Veverka, J., and C. Sagan, 1974. McLaughlin and Mars, *American Scientist, 62,* 44-53.

Ward, W., 1974. Climate variations on Mars 1. astronomical theory of insolation, *J. Geophys. Res., 79,* 3375-3385.

White, B.R., 1979. Soil transport by wind on Mars, *J. Geophys. Res., 84,* 4643-4651.

White, B.R., R. Greeley, J.D. Iversen, and J.B. Pollack, 1976. Estimated grain saltation in a Martian atmosphere, *J. Geophys. Res., 81,* 5643-5650.

White, B.R., and J.C. Schulz, 1977. Magnus effect in saltation, *J. Fluid Mech., 81,* no. 3, 497-512.

Whitney, M.I., and R.V. Dietrich, 1973. Ventifact sculpture by windblown dust, *Geol. Soc. Am. Bull., 84,* 2561-2582.

Whitney, M.I., 1979. Electron micrography of mineral surfaces subject to wind-blast erosion, *Geol. Soc. Am. Bull.,* part 1, *90,* 917-934.

Williams, S.H., 1981. Calculated and inferred aeolian abrasion rates: Earth and Mars, M.S. thesis, Ariz. State Univ., Tempe.

1. Report No.	2. Government Accession No.	3. Recipient's Catalog No.
NASA CR-3788		

4. Title and Subtitle	5. Report Date
ABRASION BY AEOLIAN PARTICLES: EARTH AND MARS	March 1984
	6. Performing Organization Code: EL-4

7. Author(s)	8. Performing Organization Report No.
R. Greeley, S. Williams, B. R. White, J. Pollack, J. Marshall, and D. Krinsley	
	10. Work Unit No.

9. Performing Organization Name and Address	11. Contract or Grant No.
Planetary Geology Group Department of Geology Arizona State University Tempe, AZ 85287	NSG-2284 and NCC2-60
	13. Type of Report and Period Covered: Contractor Report

12. Sponsoring Agency Name and Address	14. Sponsoring Agency Code
Office of Space Science and Applications National Aeronautics and Space Administration Washington, DC 20546	

15. Supplementary Notes

R. Greeley: Arizona State University, Tempe, Arizona.
S. Williams: University of Santa Clara, Santa Clara, California.
B. R. White: University of California at Davis, Davis, California.
J. Pollack: NASA Ames Research Center, Moffett Field, California.
J. Marshall and D. Krinsley: Arizona State University, Tempe, Arizona.

NASA Technical Monitor: Joseph M. Boyce

Summary Report

16. Abstract

Estimation of the rate of aeolian abrasion of rocks on Mars requires knowledge of (1) particle flux, (2) susceptibilities to abrasion of various rocks, and (3) wind frequencies on Mars. Fluxes and susceptibilities for a wide range of conditions were obtained in the laboratory and combined with wind data from the Viking meteorology experiment. Assuming an abundant supply of sand-sized particles, estimated rates range up to 2.1×10^{-2} cm of abrasion per year in the vicinity of Viking Lander 1. This rate is orders of magnitude too great to be in agreement with the inferred age of the surface based on models of impact crater flux. The discrepancy in the estimated rate of abrasion and the presumed old age of the surface cannot be explained easily by changes in climate or exhumation of ancient surfaces. We consider the primary reason to be related to the agents of abrasion. Either windblown grains are in very short supply, or the grains are ineffective as agents of abrasion. At least some sand-sized ($\sim$100 μm) grains appear to be present, as inferred from both lander and orbiter observations. High rates of abrasion occur for all experimental cases involving sands of quartz, basalt, or ash. However, previous studies have shown that sand is quickly comminuted to silt- and clay-sized grains in the martian aeolian regime. Experiments also show that these fine grains are electrostatically charged and bond together as sand-sized aggregates. Laboratory simulations of wind abrasion involving aggregates show that at impact velocities capable of destroying sand, aggregates form a protective veneer on the target surface and can give rise to extremely low abrasion rates.

17. Key Words (Suggested by Author(s))	18. Distribution Statement
Mars Venus Earth Aeolian Eolian Erosion Abrasion Geology	Unclassified - Unlimited Subject Category 25

19. Security Classif. (of this report)	20. Security Classif. (of this page)	21. No. of Pages	22. Price
Unclassified	Unclassified	50	A03

For sale by the National Technical Information Service, Springfield, Virginia 22161

NASA-Langley, 1984